

Adaptive Mesh Refinement for Characteristic Grids

Jonathan Thornburg

13 May 2010

Abstract I consider techniques for Berger-Oliger adaptive mesh refinement (AMR) when numerically solving partial differential equations with wave-like solutions, using characteristic (double-null) grids. Such AMR algorithms are naturally recursive, and the best-known past Berger-Oliger characteristic AMR algorithm, that of Pretorius & Lehner (*J. Comp. Phys.* **198** (2004), 10), recurses on individual “diamond” characteristic grid cells. This leads to the use of fine-grained memory management, with individual grid cells kept in 2-dimensional linked lists at each refinement level. This complicates the implementation and adds overhead in both space and time. Here I describe a Berger-Oliger characteristic AMR algorithm which instead recurses on null *slices*. This algorithm is very similar to the usual Cauchy Berger-Oliger algorithm, and uses relatively coarse-grained memory management, allowing entire null slices to be stored in contiguous arrays in memory. The algorithm is very efficient in both space and time. I describe discretizations yielding both 2nd and 4th order global accuracy. My code implementing the algorithm described here is included in the electronic supplementary materials accompanying this paper, and is freely available to other researchers under the terms of the GNU general public license.

PACS 04.25.Dm, 02.70.-c, 02.70.Bf, 02.60.Lj

Keywords adaptive mesh refinement, finite differencing, characteristic coordinates, characteristic grids, Berger-Oliger algorithm

This paper is dedicated to the memory of Thomas Radke, my late friend, colleague, and partner in many computational adventures.

1 Introduction

Adaptive mesh refinement (AMR) algorithms are now a vital part of computational science and are particularly valuable in the numerical solution of partial differential equations (PDEs) whose solutions have a wide dynamic range across the problem domain. Here I focus on explicit finite difference methods and PDEs which have propagating-wave solutions.

Department of Astronomy, Indiana University, Bloomington, Indiana, USA,
E-mail: jthorn@astro.indiana.edu

The most powerful and general AMR algorithms for problems of this type are those based on the pioneering work of Berger and Oliger (1984) (see also Berger (1982, 1986); Berger and Colella (1989)). These algorithms use locally uniform grids, refined in space and time as needed, with fine grids (which generally cover only a small part of the problem domain) overlaying coarse grids. At each time step, coarse grids are integrated first and spatial boundary conditions for fine-grid integrations are obtained by time-interpolation from the coarse grids. This whole process is applied recursively at each of the possibly-many levels of mesh refinement.

Berger and Oliger’s original work, as well as most following work, used Cauchy-type coordinates and grids, where initial data is given on a spacelike hypersurface and the solution is then computed one spacelike slice at a time within a numerical problem domain with (typically) timelike boundaries. For problems where the propagating-wave PDEs are naturally posed on an infinite domain, these finite-domain timelike boundaries require radiation boundary conditions. For many problems of interest these boundary conditions can only be approximate, and for the Einstein equations or similar constrained PDE systems they may render the evolution system ill-posed, generate significant boundary reflections, and/or generate significant constraint violations. In practice it’s often difficult and/or computationally expensive to reduce these boundary-condition errors to an acceptably low level.¹

As an alternative to Cauchy formulations, here I consider *characteristic* formulations, where the numerical problem domain’s boundaries are null geodesics. This makes it very easy to impose boundary conditions on the continuum PDEs in a well-posed and constraint-preserving manner, and to approximate these boundary conditions very accurately in the finite differencing scheme. While Cauchy-type AMR is now widely used in numerical relativity, and characteristic formulations are also not uncommon, there has been much less study of Berger-Oliger AMR using characteristic formulations. This is the topic of this paper.

The best-known work on Berger-Oliger characteristic AMR is that of Pretorius and Lehner (2004), who describe an algorithm which treats the two null coordinates symmetrically, and whose fundamental unit of recursion is the “diamond” double-null characteristic grid cell. This leads to their code using very fine-grained memory management, with each individual grid point at each refinement level containing linked-list pointers to its neighboring grid points in each null direction. This makes the programming more complicated and adds some space and time overhead. Their algorithm has $\mathcal{O}(\Delta^2)$ global accuracy, where Δ is the grid resolution.

In contrast, the AMR algorithm I describe here is much closer to the earlier work of Hamadé and Stewart (1996), treating the two null coordinates asymmetrically and only recursing on null *slices*. (In Cauchy-evolution terms, the slice-recursion algorithm treats one null coordinate as a “time” coordinate labelling null slices and the other as a “space” coordinate labelling events on a null slice.) My algorithm uses relatively coarse-grained memory management, with all the grid points in a single null slice level stored in a single set of arrays which can easily be stored contiguously in memory. This leads to relatively simple programming with only a small loss of efficiency from the coarser-grained adaptivity. I describe finite differencing schemes and interpolation operators which yield $\mathcal{O}(\Delta^4)$ global accuracy, as well as the usual $\mathcal{O}(\Delta^2)$. By using C++ templates, my code is able to support both cases with no run-time overhead.

¹ See Givoli (1991) for a general review of numerical radiation boundary conditions, and Kidder *et al.* (2005); Rinne (2006); Buchman and Sarbach (2006, 2007); Rinne *et al.* (2007); Ruiz *et al.* (2007); Seiler *et al.* (2008); Rinne *et al.* (2009) for recent progress towards non-reflecting and constraint-preserving radiation boundary conditions for the Einstein equations.

To demonstrate the slice-recursion AMR algorithm I use a simple model problem, the spherically symmetric real or complex scalar wave equation on a Schwarzschild-spacetime background, with a time-dependent Dirac δ -function source term. This problem is generally representative of a wide range of black-hole perturbation problems and, more generally, of PDEs where characteristic AMR algorithms may be appropriate.

The remainder of this paper is organized as follows: the remainder of this section outlines the notation used in this paper. Section 2 describes the model problem. Section 3 gives a brief outline of the unigrid finite differencing schemes I use for globally 2nd and 4th order accuracy. Section 4 describes how the local truncation error of the finite differencing scheme can be estimated. Section 5 describes the slice-recursion AMR algorithm and compares it to other Cauchy and characteristic Berger-Oliger algorithms. Section 6 presents tests of the AMR algorithm to demonstrate that it is accurate and efficient. Section 7 draws general conclusions. Appendix A gives a detailed description of the unigrid finite differencing schemes I use. Appendix B discusses some implementation aspects of the AMR algorithm.

1.1 Notation

I generally follow the sign and notation conventions of Wald (1984), with a $(-, +, +, +)$ metric signature. I use the Penrose abstract-index notation, with Latin indices abc running over spacetime coordinates. ∇_a is the covariant derivative operator associated with the 4-metric.

I use upper-case sans-serif letters A, B, C, ... to label grid points and (in section 5 and appendix A) finite difference grids. I describe my notation for finite difference grids in detail in section 5.1. I use SMALL CAPITALS for the names of software packages and (in appendix B.4) major data structures in my AMR code. $\lceil x \rceil$ denotes the smallest integer $\geq x$.

I use a pseudocode notation to describe algorithms: Lines are numbered for reference, but the line numbers are not used in the algorithm itself. # marks comment lines, while keywords are typeset in **bold font** and most variable names in *typewriter font* (a few variable names are mathematical symbols, such as " ℓ_{\max} "). " $X \leftarrow Y$ " means that the variable X is assigned the value of the expression Y . Variables are always declared before use. The declaration of a variable explicitly states the variable's type and may also be combined with the assignment of an initial value, as in "**integer** $j \leftarrow 0$ ". The looping construct "**for integer** x **from** A **to** B **by** C " is inspired by BASIC but also includes a declaration of the loop variable (with scope limited to the loop body, as in C++ and Perl). The looping semantics are the same as Fortran's "**do** $X = A, B, C$ ", with the increment C defaulting to 1 if omitted. Conditional statements use PL/I-inspired syntax (**if-then-else**). { and } delimit the scope of procedures, loop bodies, and either of the branches of conditional statements. Procedures (subroutines) are marked with the keyword **procedure**, and are explicitly invoked with a **call** statement. Procedure names are typeset in *typewriter font*. When referring to a procedure as a noun in a figure caption or in the main text of this paper, the procedure name is suffixed with " $()$ ", as in " $\text{foo}()$ ".

2 Model Problem

The basic AMR algorithm presented here is quite general, but for ease of exposition I present it in the context of a simple model problem. This model problem derives from the calculation of the radiation-reaction "self-force" on a scalar particle orbiting a Schwarzschild black hole,

but for purposes of this paper the model problem may be considered by itself, divorced from its physical context.

Thus, consider Schwarzschild spacetime of mass M and introduce ingoing and outgoing null coordinates u and v respectively, so the line element is

$$ds^2 = -f(r)dudv + r^2 d\Omega^2, \quad (1)$$

where r is (thus defined to be) the usual areal radial coordinate, $f(r) \equiv 1 - 2M/r$, and $d\Omega^2$ is the line element on a 2-sphere of constant r . It's also useful to define the Schwarzschild time coordinate $t_{\text{Schw}} = \frac{1}{2}(v + u)$ and the “tortoise” radial coordinate

$$r_* = \frac{1}{2}(v - u) = r + 2M \log \left| \frac{r}{2M} - 1 \right|. \quad (2)$$

In this paper I only consider the region outside the event horizon, $r > 2M$, so the coordinates t_{Schw} , r , and r_* are always nonsingular, t_{Schw} is always timelike, and both r and r_* are always spacelike. My computational scheme requires numerically inverting (2) to obtain $r(r_*)$; I discuss this inversion in appendix B.1.

The model problem is the spherically symmetric scalar wave equation on this background spacetime, with a time-dependent Dirac δ -function source term (stationary in space),

$$\square\phi + V(r)\phi \equiv \frac{\partial^2 \phi}{\partial u \partial v} + V(r)\phi = S(t_{\text{Schw}})\delta(r - r_p), \quad (3)$$

where $\square = \nabla^a \nabla_a$ is the usual curved-space wave operator, ϕ is a real or complex scalar field, $r_p > 2M$ is a specified “particle” radius giving the spatial position of the source-term worldline, $V(r)$ is a specified (smooth) position-dependent potential which varies on a typical spatial scale $\gtrsim M$ and which vanishes at spatial infinity, and $S(t_{\text{Schw}})$ is a specified time-dependent (typically highly-oscillatory) source term defined along the source worldline $r = r_p$.

I define $\|\cdot\|$ to be a pointwise norm on the scalar field ϕ . For reasons discussed in section 4.2, in the complex-scalar-field case $\|\cdot\|$ should be the complex magnitude rather than (say) the L_1 norm $\|\phi\|_1 = |\text{Re}[\phi]| + |\text{Im}[\phi]|$, even though the latter is slightly cheaper to compute.

As shown in figure 1, the problem domain is a square in (v, u) space, $(v, u) \in [v_{\min}, v_{\max}] \times [u_{\min}, u_{\max}]$. I take the particle worldline $r = r_p$ to symmetrically bisect the domain. For a given domain, it's convenient to introduce “relative v ” (rv) and “relative u ” (ru) coordinates $rv = v - v_{\min}$ and $ru = u - u_{\min}$ respectively.

Initial data must be specified along the “southwest” and “southeast” faces of the domain, $v = v_{\min}$ and $u = u_{\min}$ respectively. The “northwest” and “northeast” faces of the problem domain, $u = u_{\max}$ and $v = v_{\max}$ respectively, are ingoing null characteristics with respect to the problem domain, so no boundary conditions need be posed there. This is a key advantage of a characteristic evolution scheme. In contrast, using a Cauchy evolution scheme an outgoing-radiation boundary condition is generally required on each timelike boundary.

Assuming smooth initial data on the southwest and southeast grid faces, ϕ is C^∞ everywhere in the problem domain except at the particle worldline. In practice, ϕ and its spacetime gradients display high dynamic ranges across the problem domain, varying rapidly near the particle worldline but only slowly far from the worldline. This makes a unigrid scheme quite inefficient and is the primary motivation for using AMR.

Because of the δ -function source term, at the particle worldline ϕ is generically only C^1 , i.e., ϕ is continuous but its gradient generically has a jump discontinuity across the particle worldline. Any finite differencing or interpolation operators which include grid points on both sides of the particle worldline must take the discontinuity into account.

3 Unigrid Finite Differencing

The foundation of any mesh-refinement scheme is a stable and locally consistent unigrid discretization. To describe this, I introduce a uniform finite-difference grid over the problem domain, with equal grid spacing Δ in v and u . I use j and i as the integer grid-point coordinates corresponding to v and u respectively,

$$v_j \equiv v_{\min} + j\Delta \quad (4a)$$

$$u_i \equiv u_{\min} + i\Delta, \quad (4b)$$

where j and i range from 0 to $N \equiv D/\Delta$ inclusive, where $D = v_{\max} - v_{\min} = u_{\max} - u_{\min}$ is the problem-domain size. As is common in finite-differencing computations, I use the notation that subscripting a grid function denotes its value at the specified grid point, for example

$$\phi_{j,i} \equiv \phi(v=v_j, u=u_i). \quad (5)$$

To simplify the finite differencing near the particle worldline, I require that the grid be placed such that if the particle worldline passes through a grid cell, it does so symmetrically, bisecting through the center of the cell.² This assumption considerably simplifies the finite differencing near the particle worldline, and makes it easy to represent the effects of the δ -function source term accurately. (See Tornberg and Engquist (2004) for a general discussion of the numerical treatment of δ -function terms in PDEs.)

The finite difference schemes I consider here are all explicit, with molecules summarized in figure 2. Briefly, for 2nd order global accuracy I use a standard diamond-cell integration scheme (Gómez and Winicour (1992); Gómez *et al.* (1992); Gundlach *et al.* (1994); Burko and Ori (1997); Lousto and Price (1997); Lousto (2005); Winicour (2009)), while for 4th order global accuracy I use a modified version of the scheme described by Lousto (2005); Haas (2007). I describe the finite differencing schemes in detail in appendix A. With one exception discussed in appendix A.3, these finite differencing schemes are stable.

² This symmetric passage is only possible because r_p is time-independent. For the more generic case where r_p is time-dependent, then in general the particle worldline would pass obliquely through the cell. As discussed by, for example, Martel and Poisson (2002); Lousto (2005); Haas (2007), this would considerably complicate the finite differencing of cells intersecting the particle worldline. However, it wouldn't alter the overall character of the AMR algorithm.

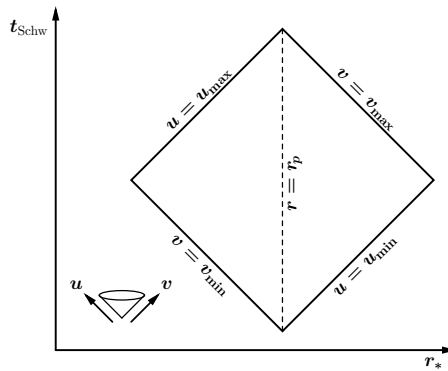


Fig. 1 This figure shows the overall problem domain, and the (u, v) and (t_{Schw}, r_*) coordinates. The vertical dashed line marks the particle worldline.

It's important to know the domain of dependence of the finite difference computation of $\phi_{j,i}$, i.e., the set of grid points $(j+\beta, i+\alpha)$ where $\phi_{j+\beta, i+\alpha}$ is used as an input in computing $\phi_{j,i}$. (I define the “radius” of such a finite difference computation as the maximum of all such $|\beta|$ and $|\alpha|$, the radius in the j direction as the maximum of all such $|\beta|$, and the radius in the i direction as the maximum of all such $|\alpha|$.) For 2nd order global accuracy, the domain of dependence is precisely that shown in figure 2, i.e., it comprises the 3 grid points $\{(j, i-1), (j-1, i), (j-1, i-1)\}$. For 4th order global accuracy, this set depends on the position of (j, i) relative to the particle worldline, but it never includes points outside the 4 slices $\{j, j-1, j-2, j-3\}$ or outside the 4 u positions $\{i, i-1, i-2, i-3\}$.

Given this domain of dependence, there are many possible orders in which the $\phi_{j,i}$ may be computed in a unigrid integration. However, the algorithms I consider here all integrate the grid points in “raster-scan” order, i.e., using an outer loop over j (so that each iteration of the outer loop integrates a single $v = \text{constant}$ null slice) and an inner loop over i .

3.1 Local versus Global Truncation Errors for Characteristic Schemes

Recall the (standard) definitions of the local and global truncation error of a finite differencing scheme (Kreiss and Oliger (1973); Choptuik (1991); Richtmyer and Morton (1994); LeVeque (2007)): The local truncation error (LTE) is a pointwise norm of the discrepancy that results when the exact solution of the PDE is substituted into the finite difference equations at a grid point. The global truncation error (GTE) is a pointwise norm of the difference between the exact solution of the PDE and the result of solving the finite difference equations using exact arithmetic (i.e., without floating-point roundoff errors). The LTE and GTE are both grid functions.

For a stable and consistent Cauchy evolution scheme, the GTE and LTE are normally of the same order in the grid spacing Δ (Kreiss and Oliger (1973); Choptuik (1991); Richtmyer and Morton (1994); LeVeque (2007)). However, in a characteristic evolution, errors can build up cumulatively over many grid points, so the GTE is generically worse than the LTE. For a 1+1 (space+time) dimensional problem such as that considered here, errors can accumulate over $\mathcal{O}(N^2)$ grid points where $N = \mathcal{O}(1/\Delta)$, so generically an $\mathcal{O}(\Delta^{n+2})$ LTE is required to guarantee an $\mathcal{O}(\Delta^n)$ GTE. Corresponding to this, the finite differencing schemes

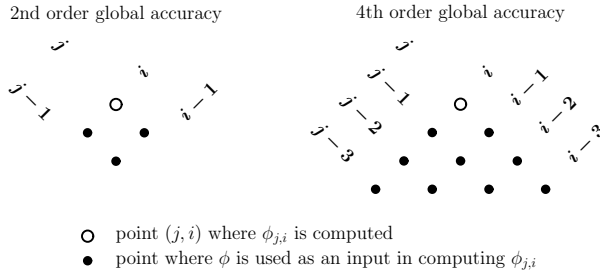


Fig. 2 This figure summarizes the unigrid finite differencing molecules. The left subfigure shows the molecule used for 2nd order global accuracy. The right subfigure shows the molecule used for 4th order global accuracy far from the particle worldline; near the worldline the molecules are more complicated, and are shown in figure 10. Open circles show the point where ϕ is being computed; solid circles show points where ϕ is used as an input in the computation of $\phi_{j,i}$.

I present here for 2nd and 4th order global accuracy (GTE) actually have 4th and 6th order LTE respectively, except near the particle worldline where one order lower GTE is acceptable because there are only $\mathcal{O}(N)$ near-worldline grid cells.

3.2 Initial Data

The globally-4th-order finite differencing scheme summarized in figure 2 and described in detail in appendix A.2 is a 4-level scheme: the finite-difference molecule for computing $\phi_{j,i}$ includes points on 3 previous slices and at 3 previous u positions. Physical boundary conditions are (only) given on the southeast and southwest grid boundaries, so starting the numerical integration requires that “extended initial data” somehow be computed, comprising the physical boundary data, the next 2 slices after the southwest grid boundary, and the next 2 grid points on each succeeding slice after the southeast grid boundary. I describe several different schemes for constructing the extended initial data in appendix A.2.4.

4 Estimation of the Local Truncation Error

As is common in AMR algorithms, I implement the “adaptive” part of AMR using an estimate of the numerical solution’s local truncation error (LTE). I compute this via the standard technique (LeVeque (2007, section A.6)) of comparing the main numerical integration with that from a coarser-resolution integration. In the context of Berger-Oliger style AMR, where a hierarchy of grids are being integrated concurrently at varying resolutions, there are several possible choices for the coarser-resolution comparison solution. It can come from a separate “shadow” AMR hierarchy (each level of which is coarser than the corresponding level of the main AMR hierarchy), or it can come from the next-coarsest level of the (single) AMR hierarchy (the “self-shadow hierarchy” technique of Pretorius (2002b); Pretorius and Lehner (2004)).

Here I use a different technique, also used by Hamadé and Stewart (1996), where the coarser-resolution comparison is obtained locally within the (unigrid) evolution at each level of the grid hierarchy, by simply subsampling every 2nd grid point of every 2nd slice. That is, suppose we have a finite differencing scheme with $\mathcal{O}(\Delta^n)$ LTE, whose domain of dependence for computing $\phi_{j,i}$ is the set of K grid points $\{(j+\beta_k, i+\alpha_k) | 1 \leq k \leq K\}$ for some constants $\{\beta_k\}$ and $\{\alpha_k\}$. For any (j, i) and Δ , let $\phi_{j,i}^{(\Delta)}$ be the value of $\phi_{j,i}$ obtained from the usual numerical integration with grid spacing Δ . Let $\phi_{j,i}^{(\Delta \rightarrow 2\Delta)}$ be the value of $\phi_{j,i}$ obtained by taking a single step of size 2Δ using as inputs the $\phi_{j,i}^{(\Delta)}$ values at the set of K grid points $\{(j+2\beta_k, i+2\alpha_k) | 1 \leq k \leq K\}$. Then I estimate the LTE in computing $\phi_{j,i}^{(\Delta)}$ as

$$\text{LTE} \approx \frac{1}{2^n - 4} \left\| \phi_{j,i}^{(\Delta)} - \phi_{j,i}^{(\Delta \rightarrow 2\Delta)} \right\| \quad (6)$$

where the normalization factor is obtained by comparing the LTE of a single 2Δ -sized step with that accumulated in 4 separate Δ -sized steps covering the same region of spacetime.

This scheme is easy to implement and works well, although it does limit the locations where the LTE can be estimated to those where (i) the data for a 2Δ -sized step is available, and where (ii) both the Δ - and 2Δ -sized steps use the same finite differencing scheme. Constraint (i) implies, for example, that when a new refinement level is created, LTE estimates

aren't available for it until a few $v = \text{constant}$ slices have been integrated on that level. For the finite differencing schemes described here, constraint (ii) implies that the LTE estimate isn't available for cells within a few grid points of the particle worldline. I haven't found either of these constraints to be a problem in practice.

4.1 Cost of Computing the LTE Estimate

The cost in space (memory usage) associated with this LTE-estimation scheme is the requirement that sufficiently many adjacent slices be kept in memory simultaneously for the 2Δ -sized steps. For the globally-2nd-order finite differencing scheme described in section 3, the LTE estimator requires data from 3 adjacent slices. As discussed in section 5.3, for 2nd order global accuracy my AMR algorithm uses interpolation operators which use data from up to 4 adjacent slices, so the LTE estimator is “free” in the sense that it doesn't increase the number of slices needing to be kept in memory beyond what the rest of the computation already requires. For the globally-4th-order finite differencing scheme described in section 3, the LTE estimator requires 7 adjacent slices, while the interpolation operators only need 6 adjacent slices, so the LTE estimator adds a $\frac{1}{6} \approx 17\%$ fractional overhead in memory usage.

I discuss the CPU-time cost of computing the LTE estimate in footnote 9 in section 5.3.

4.2 Smoothing the LTE Estimates

In an AMR scheme, mesh-refinement boundaries and regridding operations tend to introduce small amounts of interpolation noise into the numerical solution, which tends to be amplified in the LTE estimate. In particular, for the scheme described here, there are often isolated points with anomalously high LTE estimates. To avoid having these falsely trigger (unwanted) mesh refinements, I smooth the LTE estimates on each slice with a moving median-of-3 filter before comparing them to the error threshold.

Pretorius and Lehner (2004) describe the use of a moving-average smoothing of the LTE estimate to address a slightly different problem in their characteristic AMR algorithm:

The point-wise TE [truncation error] computed using solutions to wave-like finite-difference equations is in general oscillatory in nature, and will tend to go to zero at certain points within the computational domain ..., even in regions of relatively high truncation error. We do not want such isolated points of (anomalously) small TE to cause temporary unrefinement, ...

For the model problem I consider here, “temporary unrefinement” doesn't seem to be a problem in practice so long as the norm $\|\cdot\|$ is chosen to be the complex magnitude of ϕ . This appears to be because while the complex phase of ϕ oscillates rapidly along the particle worldline, ϕ 's complex magnitude tends to remain relatively constant. (In an early version of my AMR code where I used the L_1 norm $\|\phi\|_1 = |\text{Re}[\phi]| + |\text{Im}[\phi]|$, I found that temporary unrefinement did indeed tend to occur, as the rapidly changing complex phase of ϕ translated into corresponding changes in $\|\phi\|_1$.)

For other physical systems, further smoothing of the estimated LTE might be necessary.

5 Adaptive Mesh Refinement

5.1 The Berger-Oliger Algorithm

The Berger-Oliger AMR algorithm for Cauchy evolutions of hyperbolic or hyperbolic-like PDEs (Berger and Oliger (1984); see also Berger (1982, 1986); Berger and Colella (1989)) was first used in numerical relativity by Choptuik (1986, 1989, 1992, 1993), and is now widely used for a variety of problems. Schnetter *et al.* (2004) give a nice summary of some of the considerations involved in using the Berger-Oliger algorithm with evolution systems which contain 2nd spatial derivatives but only 1st time derivatives. Lehner *et al.* (2006); Brüggmann *et al.* (2008); Husa *et al.* (2008) discuss adjustments to the algorithm (particularly interpolation and prolongation operators) necessary to obtain higher-than-2nd-order global finite differencing accuracy in a Berger-Oliger scheme. Pretorius and Choptuik (2006) discuss refinements to the standard Berger-Oliger algorithm to accomodate coupled elliptic-hyperbolic systems of PDEs. MacNeice *et al.* (2000); Burgarelli *et al.* (2006) discuss quadtree/octtree grid structures and their use with Berger-Oliger mesh refinement. Many individual codes also have published descriptions, including (among many others), AD (Choptuik (1989, 1992, 1994)), AMRD/PAMR (Pretorius (2002b,a,c)), BAM (Brüggmann (1996); Brüggmann *et al.* (2004, 2008)), CARPET/CACTUS (Schnetter *et al.* (2004); Schnetter (2001); Goodale *et al.* (2003, 1999)), CHOMBO/AMRLIB/BOXLIB (Colella *et al.* (2009b); Su *et al.* (2006); Colella *et al.* (2009a); Rendleman *et al.* (2000); Lijewski *et al.* (2006)), the Choptuik *et al.* axisymmetric code (Choptuik *et al.* (2003a,b); Pretorius and Choptuik (2006)), HAD (Liebling (2002, 2004); Anderson *et al.* (2006)), GRACE/HDDA/AMROC/DAGH (Parashar and Li (2009); Parashar and Browne (2000); Deiterding (2006, 2005b,a); Mitra *et al.* (1995)), OVERTURE (Brown *et al.* (1999a,b); Henshaw *et al.* (2002)), PARAMESH (MacNeice *et al.* (2000); Olson and MacNeice (2005); Olson (2006); Olson and MacNeice (1999)), and SAMRAI (Hornung and Kohn (2002a, 1999); Hornung *et al.* (2006); Hornung and Kohn (2002b)).

Although the focus of this paper is on characteristic Berger-Oliger AMR, it's useful to begin with a brief review of the Cauchy Berger-Oliger algorithm. I will only present a few of the algorithm's properties that are particularly relevant here; see the references cited in the previous paragraph for more extensive discussions of the algorithm, its rationale (i.e., why the algorithm is constructed in the way that it is), and how it may be modified to meet various situations.

To describe the Berger-Oliger algorithm it's convenient to consider a generic PDE with propagating-wave solutions in 1+1 (space+time) dimensions, and define global timelike and spacelike coordinates t and x respectively.³ I consider uniform finite difference grids in these coordinates, with indices j and i indexing the t and x dimensions respectively. In contrast to the characteristic-grid case discussed in section 3, I don't assume that the grid cells are square, i.e., I don't assume anything about the Courant number (the ratio of the time step to the spatial resolution).

The basic data structure of the Berger-Oliger algorithm is that of a hierarchy of such uniform grids, each having a different resolution. The grids are indexed by an integer "refinement level" ℓ in the range $0 \leq \ell \leq \ell_{\max}$. (In general ℓ_{\max} is time-dependent, but for convenience I don't explicitly show this in the notation.) I refer to the grid at refinement level ℓ as $G^{(\ell)}$, to the time level ("slice") j (i.e., the slice $t = t_j$) of $G^{(\ell)}$ as $G_j^{(\ell)}$, to the grid point $(t=t_j, x=x_i)$ as (j, i) , and to the grid function value(s) at this grid point as $G_{j,i}^{(\ell)}$. In general

³ For the model problem of section 2 these coordinates may be taken to be $t = t_{\text{Schw}}$ and $x = r_*$.

any $G_j^{(\ell)}$ may consist of several connected components, but here I focus on the simpler case where each $G_j^{(\ell)}$ contains only a single connected component⁴ covering some closed interval $x \in [G_j^{(\ell)}.x_{\min}, G_j^{(\ell)}.x_{\max}]$, with corresponding grid-point indices $i \in [G_j^{(\ell)}.i_{\min}, G_j^{(\ell)}.i_{\max}]$. As suggested by the notation, in general the domain of $G^{(\ell)}$ isn't rectangular, i.e., in general $G_j^{(\ell)}.x_{\min}$, $G_j^{(\ell)}.x_{\max}$, $G_j^{(\ell)}.i_{\min}$, and $G_j^{(\ell)}.i_{\max}$ all vary with j .

The coarsest or “base” grid $G^{(0)}$ covers the entire problem domain. For each integer ℓ with $0 < \ell \leq \ell_{\max}$, $G^{(\ell)}$ has a resolution 2^ℓ times finer than that of $G^{(0)}$,⁵ and typically covers only some proper subset of the problem domain. Here I consider only “vertex-centered” grids, where every 2nd $G^{(\ell+1)}$ point coincides with a $G^{(\ell)}$ point.⁶ The Berger-Oliger algorithm requires that the grids always be maintained such that for any ℓ , on any slice common to both $G^{(\ell)}$ and $G^{(\ell+1)}$, the region of the problem domain covered by $G^{(\ell+1)}$ is a (usually proper) subset of that covered by $G^{(\ell)}$. I refer to this property as the “proper nesting” of the grids.⁷

Each grid $G^{(\ell)}$ maintains its own current slice for the integration, denoted $G_{\text{current},j}^{(\ell)}$; the j coordinate of this slice is denoted $G^{(\ell)}.current_j$. Each slice is integrated with the same finite differencing scheme and Courant number.⁸ Although I describe each $G^{(\ell)}$ here as containing the entire time history of its integration, in practice only the most recent few time slices need to be stored in memory. The precise number of time slices needed is set by the larger of the number needed by the unigrid finite differencing scheme, the LTE estimation, and by the interpolations used in the Berger-Oliger algorithm. This is discussed further in section 5.3.

Figure 3 (ignoring the lines marked with \bullet , whose purpose will be discussed in section 5.3) gives a pseudocode outline of the Berger-Oliger algorithm. Notice that the algo-

⁴ For the model problem of section 2 this isn't a significant restriction, since apart from the (ignorable) spurious radiation discussed in section 5.3.1, the resolution required to adequately represent ϕ tends to decrease monotonically with distance from the particle worldline, so that for a given LTE threshold, the region of a slice needing a given resolution is just a single closed interval. For other problems this might not be the case, requiring some or all of the $G_j^{(\ell)}$ to have multiple connected components for good efficiency. This would somewhat complicate the data structures, but it wouldn't alter the overall character of the AMR algorithm.

⁵ This can easily be generalized to any other integer refinement ratio > 1 (including having the refinement ratio vary from one level to another). Larger refinement ratios reduce the ℓ_{\max} needed for a given total dynamic range of resolution in the refinement hierarchy and thus reduce some of the “bookkeeping” overheads in the computation. However, smaller refinement ratios give a smoother variation of the grid resolution (i.e., a variation with smaller jumps) across the problem domain, allowing the resolution to be better matched to that needed to just obtain the desired LTE at each event, which improves the overall efficiency of the computation. For this latter reason I use a refinement ratio of 2:1 in my AMR algorithm and code.

⁶ An alternative approach uses “cell-centered” grids, where grid points are viewed as being at the center of grid cells and it is these grid *cells* which are refined (so that the $G^{(\ell+1)}$ grid points are located $\frac{1}{4}$ and $\frac{3}{4}$ of the way between adjacent $G^{(\ell)}$ grid points). This approach is particularly useful with finite volume discretizations (LeVeque (2002)) and is used by, for example, the PARAMESH mesh-refinement framework (MacNeice *et al.* (2000); Olson and MacNeice (2005); Olson (2006); Olson and MacNeice (1999)) and the BAM code (Brügmann *et al.* (2004, 2008)).

⁷ The proper-nesting requirement is actually slightly stronger: each $G^{(\ell+1)}$ grid point must be far enough inside the region covered by $G^{(\ell)}$ to allow interpolating data from $G^{(\ell)}$. In practice, in the v direction this requirement is enforced implicitly by the Berger-Oliger algorithm, while in the u direction this requirement must be enforced explicitly in the regridding process (procedure `shrink_to_ensure_proper_nesting()` in figure 4).

⁸ Using the same Courant number at each refinement level (i.e., scaling the time step on each grid proportional to the spatial resolution) is known as “subcycling in time” and is widely, though not universally, used in Berger-Oliger AMR codes. Dursi and Zingale (2003) discuss some of the tradeoffs determining whether or not subcycling is worthwhile.

rithm is recursive, and that this recursion is at the granularity of an entire slice. That is, the algorithm integrates an entire slice (lines 11–19 in figure 3) before recursing to integrate the finer grids (if any).

A key part of the Berger-Oliger algorithm is regridding (lines 23–28 in figure 3), where the grid hierarchy is updated so that each $G^{(\ell)}$ covers the desired spatial region for the current time. As shown in more detail in figure 4, if this requires adding a new $G^{(\ell)}$ to the hierarchy, or moving an existing $G^{(\ell)}$ to cover a different set of spatial positions than it previously covered, then data must be interpolated from coarser refinement levels to initialize the new fine-grid points. Finer grids may also need to be updated to maintain proper nesting. Because of this, and because of the data copying discussed below, regridding is moderately expensive, typically costing $\mathcal{O}(1)$ times as much (at each level of the refinement hierarchy) as integrating a single time step. To prevent this cost from dominating the overall computation, regridding is only done on “selected” slices; in practice a common choice is to regrid on every k th slice at each level of the refinement hierarchy, for some (constant) parameter $k \sim 4$. For similar reasons, the LTE estimate is often only computed at every k th grid point.⁹

Figure 5 shows an example of the operation of the slice-recursion algorithm discussed in section 5.3. However, parts (a)–(e) of this figure can also be interpreted as an example of the operation of the (Cauchy) Berger-Oliger algorithm discussed in this section, with u as the spatial coordinate and v as the time coordinate. [The example shown is unrealistic in one way: to allow the figure to show a relatively small number of grid points (and thus be at a larger and more legible scale), the figure ignores the limits on regridding discussed in section 5.3.1, which my code actually enforces.]

Because the globally-4th-order finite differencing scheme illustrated in figure 5 is a 4-level scheme, the extended initial data for the base grid comprises 3 slices and 3 points on each succeeding slice. Figure 5a shows the base grid just after the computation of the first evolved point of its first evolved slice (i.e., the first slice which isn’t entirely part of the extended initial data).

Figure 5b shows an example of the LTE being checked at several points, and (after smoothing) exceeding the error threshold at one of these. The regridding procedure thus creates a new fine grid (lines 18–22 in figure 4). Figure 5c shows this new fine grid just after the computation of the first evolved point of its first evolved slice. Notice that the actual spatial extent of the newly-created fine grid is larger than just the set of points where the (smoothed) LTE exceeds the error threshold, for two reasons:

- If the (smoothed) LTE estimate exceeds the error threshold at some location on the current slice, then logically we don’t know which point(s) in the LTE-estimate molecule have inaccurate data. The algorithm thus includes *all* the LTE-estimate molecule’s points in the region-to-be-refined (line 18 of figure 3).
- The algorithm also uses “buffer zones” to further enlarge the region-to-be-refined in the spatial direction beyond the set of points just described (lines 20–21 in figure 3). The buffer zones are 2 grid points on each side of this set for the example shown in figure 5c. The buffer zones are used for two reasons:
 - The buffer zones ensure that moving solution features and their finite-difference domains of dependence will remain within the refined region – and thus be well-resolved – throughout the time interval before the next regridding operation.

⁹ The LTE estimate discussed in section 4 roughly doubles the cost of integrating a single grid point, so estimating the LTE at every k th grid point of every k th slice adds a fractional overhead of roughly $1/k^2$ to the computation. For $k = 4$ (the example shown in figure 5b) this is only about 6%.

- The buffer zones also help to ensure that if there are any finer grids in the grid hierarchy, the finite-difference domains of dependence for interpolating the next-finer grid’s spatial boundary data from the current grid (line 9 in figure 3; figure 5c,d) will avoid regions where the solution is not well-resolved by the current grid (and hence the interpolation would be inaccurate).

When a new fine grid $G^{(\ell+1)}$ is created, at what time level should it be placed relative to the next-coarser grid $G^{(\ell)}$? There are a number of possible design choices here, ranging from the time level of the most recent all-points-below-the-error-threshold $G^{(\ell)}$ LTE-estimate check up to the time level of the some-points-above-the-error-threshold $G^{(\ell)}$ LTE-estimate check which triggered the creation of the new fine grid. [Placing the fine grid at an earlier time level makes the total integration slightly more expensive, but lessens the use of insufficiently-accurate coarse-grid data (i.e., $G^{(\ell)}$ data whose LTE estimate exceeds the error threshold) in interpolating the fine grid’s initial data.] As shown in the example of figure 5c, I have (somewhat arbitrarily) chosen to place the newly-created fine grid $G^{(\ell+1)}$ with the last (most-future) of its initial-data slices (those which are entirely interpolated from the next-coarser grid $G^{(\ell)}$; line 20 of figure 4) at the time level $G_{\text{current}-j-1}^{(\ell)}$, one coarse-grid time step before the time level on which the over-threshold LTE estimates were computed.

Each slice $G_j^{(\ell)}$ is a standard 1-dimensional grid function or set of grid functions, and so may be stored as a contiguous array or set of arrays in memory. This is easy to program, and allows the basic time integration (lines 11–19 in figure 3) to be highly efficient.^{10,11} It also means that the amount of additional “bookkeeping” information required to organize the computation is very small, proportional only to the maximum number of distinct grids at any time. The one significant disadvantage of contiguous storage is that when regridding requires expanding $G_j^{(\ell)}$ then the existing data must be copied to a new (larger) set of arrays. However, the cost of doing this is still relatively small (less than the cost of a single time step for all the grid points involved).

After the recursive calls to integrate finer grids (lines 33 and 34 in figure 3), $G^{(\ell+1)}$ has been integrated to the same time level as $G^{(\ell)}$. Figure 5d shows an example of this. Since $G^{(\ell+1)}$ has twice as fine a resolution as $G^{(\ell)}$, it presumably represents the solution more accurately at those events common to both grids. To prevent the coarser grids from gradually becoming more and more inaccurate as the integration proceeds (which would eventually contaminate the finer grids via coarse-to-fine interpolations in regridding), the algorithm copies (“injects”) $G^{(\ell+1)}$ back to $G^{(\ell)}$ at those events common to both grids. This is done at lines 36–41 in figure 3; figure 5e shows an example of this.

5.2 The Pretorius-Lehner Algorithm

Pretorius and Lehner (2004) discuss modifications to the standard Berger-Oliger algorithm to accomodate characteristic evolution. Their algorithm treats the two null directions sym-

¹⁰ Because the algorithm primarily sweeps sequentially through contiguously-stored grid functions, it should have fairly low cache miss rates. Moreover, many modern computer systems have special (compiler and/or hardware) support for automatically prefetching soon-to-be-used memory locations in code of this type, further reducing the average memory-access time and thus increasing performance.

¹¹ In fact, with appropriate software design the basic integration routine can often be reused intact, or almost intact, from an existing unigrid code. For example, this is common when using the CARPET (Schnetter *et al.* (2004); Schnetter (2001)), PARAMESH (MacNeice *et al.* (2000); Olson and MacNeice (2005); Olson (2006); Olson and MacNeice (1999)), and SAMRAI (Hornung and Kohn (2002a); Hornung *et al.* (2006); Hornung and Kohn (2002b)) mesh-refinement infrastructures.

```

1  # integrate  $G^{(\ell)}$  forward by one time step
2  procedure time_step(integer  $\ell$ )
3  {
4   $G^{(\ell)}$ .current_j  $\leftarrow G^{(\ell)}$ .current_j + 1
5  integer j  $\leftarrow G^{(\ell)}$ .current_j
6  if ( $\ell = 0$ )
7      then set  $G_j^{(\ell)}$  spatial boundary data from the physical boundary conditions
8          and (if used) the extended initial data
9      else set  $G_j^{(\ell)}$  spatial boundary data by spacetime-interpolating from the next-coarser grid  $G^{(\ell-1)}$ 
10
11 # main integration (includes local-truncation-error estimation at selected points of selected slices)
12 region where_to_refine  $\leftarrow \emptyset$ 
13   for integer ii from  $G_j^{(\ell)}$ .i_min to  $G_j^{(\ell)}$ .i_max
14   {
15        $G_{j,ii}^{(\ell)}$   $\leftarrow$  update using the unigrid finite differencing scheme
16       if ((j is a regridding time level) and (ii is an LTE-estimation point))
17           then if (smooth(LTE_estimatej,ii) > error_threshold)
18               then where_to_refine  $\leftarrow$  where_to_refine  $\cup$  {i in LTE_estimatej,ii molecule}
19   }
20 if (where_to_refine  $\neq \emptyset$ )
21     then where_to_refine  $\leftarrow$  where_to_refine  $\cup$  buffer zones
22
23 # regrid if necessary
24 if (j is a regridding time level)
25     then call regrid( $\ell+1$ , where_to_refine)    # add, delete, and/or move  $G^{(\ell+1)}$ 
26                                             # so it covers the region where_to_refine
27                                             # (may also move or delete finer grids  $G^{(k)}$  for
28                                             #  $k > \ell+1$  in order to maintain proper nesting)
29
30 # recurse if necessary
31 if ( $G^{(\ell+1)}$  exists)
32     then {
33         call time_step( $\ell+1$ )
34         call time_step( $\ell+1$ )
35
36         # copy ("inject") fine-grid results back to coarse grid
37         integer j1  $\leftarrow G^{(\ell+1)}$ .current_j
38          $\forall$  integer i such that  $G_{j,i}^{(\ell)}$  coincides with some grid point  $G_{j1,i1}^{(\ell+1)}$  of the next-finer grid
39         {
40              $G_{j,i}^{(\ell)}$   $\leftarrow G_{j1,i1}^{(\ell+1)}$ 
41         }
42
43         • # re-integrate remainder of coarse slice
44         • integer i_max_of_fine_grid  $\leftarrow$  the  $G_j^{(\ell)}$  i coordinate which coincides with  $G_{j1}^{(\ell+1)}$ .i_max
45         •   for integer i from i_max_of_fine_grid+1 to  $G_j^{(\ell)}$ .i_max
46         •   {
47         •        $G_{j,i}^{(\ell)}$   $\leftarrow$  update using the unigrid finite differencing scheme
48         •   }
49     }
50 }
```

Fig. 3 This figure gives an outline of the standard Berger-Oliger AMR algorithm (if the lines marked with • are omitted), and of the slice-recursion algorithm (if the lines marked with • are included). See figure 4 for an outline of the procedure `regrid()` which is called at line 25.

```

1  # add, delete, and/or move  $G^{(\ell)}$  so it covers the region  $R$ 
2  # (may also move or delete finer grids  $G^{(k)}$  for  $k > \ell$  in order to maintain proper nesting)
3  procedure regrid(integer  $\ell$ , region  $R$ )
4  {
5  if (the next coarser grid  $G^{(\ell-1)}$  does not have enough time levels stored
6      to allow spacetime-interpolation from  $G^{(\ell-1)}$ )
7      then return    # ignore the regridding request for now; if the need for regridding persists,
8                      # the Berger-Oliger algorithm will keep requesting regridding, until eventually
9                      #  $G^{(\ell-1)}$  will have enough time levels stored for interpolation to be possible
10
11 if    ( $R = \emptyset$ )
12 then {
13     destroy any  $G^{(k)}$  with  $k \geq \ell$ 
14      $\ell_{\max} \leftarrow \ell - 1$ 
15 }
16
17 else if ( $G^{(\ell)}$  does not exist)
18 then {
19     create  $G^{(\ell)}$  covering the region  $R$ 
20     initialize  $G^{(\ell)}$  by spacetime-interpolating data from the next coarser grid  $G^{(\ell-1)}$ 
21      $\ell_{\max} \leftarrow \ell$ 
22 }
23
24 else {
25     move  $G^{(\ell)}$  so it covers the region  $R$ , initializing any new points
26     by spacetime-interpolating data from the next coarser grid  $G^{(\ell-1)}$ 
27     call shrink_to_ensure_proper_nesting( $\ell+1$ )
28 }
29 }
30
31 # shrink  $G^{(\ell)}$  and any finer grids as necessary so as to ensure proper nesting
32 procedure shrink_to_ensure_proper_nesting(integer  $\ell_{\min}$ )
33 {
34      $\text{max\_radius} \leftarrow$  the largest radius of any interpolation molecule in the  $i$  direction
35     for integer  $\ell$  from  $\ell_{\min}$  to  $\ell_{\max}$ 
36     {
37         integer  $j \leftarrow G^{(\ell-1)}.current\_j$ 
38         region  $R\_shrunk \leftarrow [G_j^{(\ell-1)}.i\_min + \text{max\_radius}, G_j^{(\ell-1)}.i\_max - \text{max\_radius}]$ 
39         if ( $G^{(\ell)} \not\subseteq R\_shrunk$ )
40         then {
41             region  $R\_intersection \leftarrow R\_shrunk \cap$  region covered by  $G^{(\ell)}$ 
42             if ( $R\_intersection = \emptyset$ )
43             then {
44                 destroy any  $G^{(k)}$  with  $k \geq \ell$ 
45                  $\ell_{\max} \leftarrow k - 1$ 
46                 return    # there are now no finer levels, so this procedure is done
47             }
48             shrink  $G^{(\ell)}$  to just cover the region  $R\_intersection$ 
49         }
50     }
51 }

```

Fig. 4 This figure gives an outline of the regridding procedure `regrid()` which is called by the main Berger-Oliger algorithm (figure 3), and of the auxiliary procedure `shrink_to_ensure_proper_nesting()` which is called by `regrid()`.

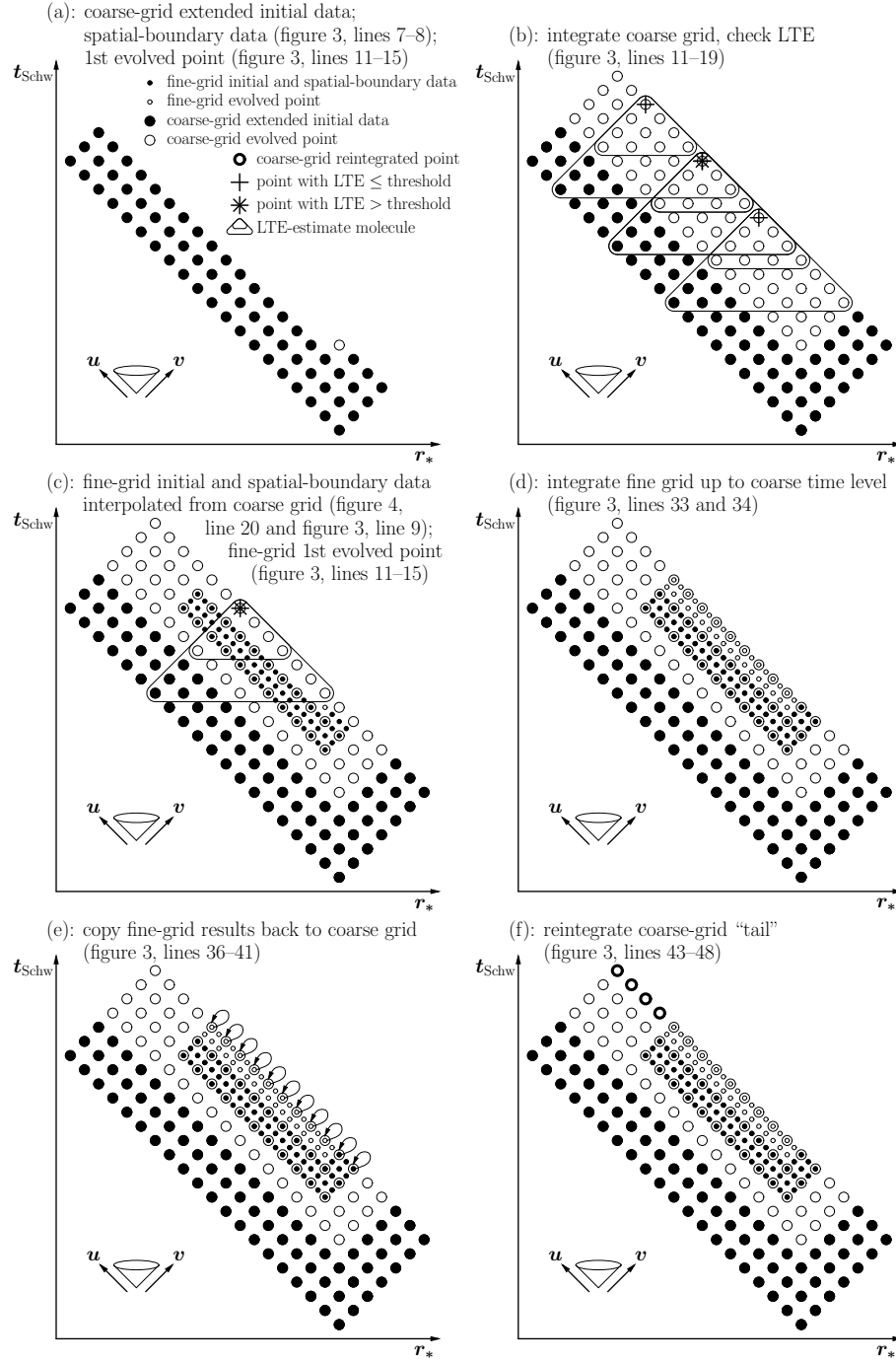


Fig. 5 This figure shows an example of the operation of the slice-recursion algorithm, using the globally-4th-order finite differencing scheme described in section 3. Parts (a)–(e) can also be interpreted as an example of the operation of the (Cauchy) Berger-Oliger algorithm, with u as the spatial coordinate and v as the time coordinate. See the main text for further discussion.

metrically, and instead of using a separate regridding step, interleaves the integration, injection, LTE estimation, and updating of the mesh-refinement hierarchy at a very fine granularity (essentially that of individual diamond cells). This gives an elegant algorithm where the integration can proceed simultaneously in both null directions, “flowing” across the problem domain in a way that’s generally not known in advance.

Because of this unpredictable flow, Pretorius and Lehner don’t use contiguous arrays to store the grid functions. Rather, they use a fine-grained linked-list data structure, where each grid point at each refinement level ℓ stores explicit pointers to its 4 (null) neighboring points at that refinement level, and also to the grid points at that same event at refinement levels $\ell \pm 1$. The Pretorius-Lehner algorithm explicitly walks these pointer chains to locate neighboring points for the (unigrid) integration at each refinement level, to create finer grids, and to inject fine-grid results back into coarser grids at each level of the refinement hierarchy.

In comparison to the contiguous storage possible with the standard (Cauchy) Berger-Oliger algorithm, this linked-list storage allocation avoids data copying when grids must be grown. However, the per-grid-point pointers require extra storage, and following the pointer chains adds some programming complexity and extra execution time.^{12,13}

5.3 The Slice-Recursion Algorithm

Here I describe a different variant of the Cauchy Berger-Oliger algorithm for characteristic evolution. The basic concept of this algorithm is to treat one null direction (v) as a “time” and the other (u) as a “space”, then apply the standard Berger-Oliger algorithm as discussed in section 5.1 (with one significant modification discussed below). Figure 3 (now including the lines marked with \bullet) gives a pseudocode outline of this “slice-recursion” algorithm, and figure 5 shows an example of the algorithm’s operation for the globally-4th-order finite differencing scheme described in section 3.

For a Cauchy evolution, the future light cone of a grid point contains only $\mathcal{O}(1)$ grid points on the next $t = \text{constant}$ slice. In contrast, for a characteristic evolution, the future light cone of a grid point (j_*, i_*) contains all points (j, i) with $j \geq j_*$ and $i \geq i_*$. To see the impact of this difference on the Berger-Oliger algorithm, suppose that on some $v = \text{constant}$ slice we have a coarser grid $G^{(\ell)}$ overlaid by a finer grid $G^{(\ell+1)}$ covering the coarse-grid coordinate region $i \in [i_1, i_2]$. Then the injection of the fine-grid results back to the coarse grid (lines 36–41 in figure 3; figure 5e) restores the coarse-grid solution to the fine-grid accuracy for $i \in [i_1, i_2]$. However, unlike in the Cauchy case, the coarse-grid solution for the slice “tail” $i > i_2$ remains inaccurate, because its computation was affected by the (inaccurate) pre-injection coarse-grid region $i \in [i_1, i_2]$. The solution to this problem is to re-integrate the “tail” $i > i_2$ of the slice after the injection (lines 43–48 of figure 3; figure 5f).

Depending on the placement of the fine grid relative to the coarse grid, the cost of the re-integration may vary from negligible up to roughly the cost of a single time step for the coarse grid (i.e., a factor of 2 increase in the cost of the coarse-grid part of the computation). This overhead only affects grids with $0 \leq \ell < \ell_{\max}$; the finest grid ($\ell = \ell_{\max}$) never needs to

¹² The largest execution-time cost is probably that due to (nearby) grid points which are accessed in succession not being in contiguous, or even nearby, memory locations. This leads to increased cache miss rates and thus poorer performance.

¹³ The execution time of the dynamic storage allocation routines themselves (C’s `malloc()` and `free()`, or other languages’ equivalents) may also be substantial. However, this can be greatly reduced by using customized storage-allocation routines that allocate grid points in large batches. These and other optimization techniques for dynamic storage allocation are discussed by, for example, Wilson *et al.* (1995); Lea (2000).

be re-integrated. In practice the re-integration overhead is generally modest; I present numerical test results quantifying this in section 6.

The slice-recursion algorithm I present here is quite similar to that outlined by Hamadé and Stewart (1996). Their algorithm shares the basic Berger-Oliger mesh-hierarchy structure, uses the same LTE estimator (section 4), imposes the same nesting requirements on the grid hierarchy, and does the same “tail” re-integration (lines 43–48 of figure 3; figure 5f). However, their algorithm uses a 4:1 refinement ratio between adjacent levels in the mesh-refinement hierarchy, whereas I use a 2:1 ratio in the slice-recursion algorithm for the reasons outlined in footnote 5. They discuss only globally-2nd-order finite differencing.

When the grid hierarchy contains 3 or more refinement levels, the evolution and regridding schemes described by Hamadé and Stewart (1996) are somewhat different than those presented here: Their algorithm integrates child grids at *all* levels of the grid hierarchy up to the same time level before doing any fine-to-coarse-grid injections (lines 36–41 of figure 3; figure 5e) or regridding (figure 4), whereas the algorithms presented here follow the standard Berger-Oliger pattern where injections and regridding are interleaved with the evolution of different refinement levels in an order corresponding to the depth-first traversal of a complete binary tree.

Unlike the algorithm of Hamadé and Stewart (1996), the slice-recursion algorithm presented here is purely recursive, treating all levels of the refinement hierarchy in exactly the same way except for the setup of the base grid’s extended initial data and the details of how the spatial boundary data are determined at the start of each slice’s integration (lines 6–9 of figure 3). An important consequence of the algorithm being organized this way is that for any integer $k \geq 1$, the algorithm’s computations on a grid hierarchy with k refinement levels are identical (apart from the initial-data setup just noted) to those in each of the recursive calls (lines 33 and 34 of figure 3) for a problem with $k+1$ refinement levels. More generally, the treatment of the k finest refinement levels in the grid hierarchy is independent of the presence of any coarser level(s). I find that this simplifies debugging, by making the algorithm’s behavior on small test problems with only a few refinement levels very similar to its behavior on large “physics” problems with many refinement levels.

Like any Berger-Oliger algorithm, the slice-recursion algorithm needs to interpolate data from coarse to fine grids (line 9 of figure 3 and lines 20 and 25–26 of figure 4, figure 5c). I use a mixture of 1-dimensional and 2-dimensional Lagrange polynomial interpolation for this, in all cases chosen so as to avoid crossing the particle worldline. Appendix B.3 describes the interpolation operators in detail. These operators may use data from up to 4 [6] adjacent slices for the 2nd [4th] order GTE schemes, which sets a lower bound on the number of slices of each $G^{(\ell)}$ which must be kept in memory. For 2nd order GTE, my code keeps only the minimum (4) number of slices in memory; for 4th order GTE, it keeps one extra slice in memory (for a total of 7) to accomodate the LTE estimator (section 4; figure 5b,c).

5.3.1 Avoiding Undesired Mesh Refinement

When adding a new refinement level to the mesh-refinement hierarchy, the interpolation of initial data (line 20 of figure 4) tends to introduce low-level noise into the field variables. The same is true when an existing fine grid is moved to a new position. In either case, this noise can cause the LTE estimate to be inaccurate. It’s thus useful to allow this noise to decay (i.e., be damped out by the inherent dissipation in the finite differencing scheme) before using the LTE estimate to determine the placement of another new refinement level. To this end, my code suppresses regridding operations for the first 8 [16] time steps of a new or newly-moved grid, for the 2nd [4th] order GTE finite differencing scheme respectively.

My code also suppresses creating a new fine grid if insufficient data is available for the interpolation of all 4 [7] slices kept in memory for the 2nd [4th] order GTE finite differencing scheme respectively.

When using the slice-recursion algorithm for the self-force computation, the arbitrary initial data on the southwest and southeast grid faces induces spurious radiation near these grid faces. This radiation is of no physical interest, so there's no need for the mesh-refinement algorithm to resolve it. Moreover, as discussed in footnote 4, not resolving the spurious radiation also allows a significant simplification of the code's data structures. Thus my code suppresses mesh refinement for the first $\sim 100M$ of the integration, and for the first $\sim 100M$ of each slice thereafter.

To reduce the effects of the interpolation noise when adding new refinement levels, my code also turns on the mesh refinement gradually, adding new refinement levels only at the rate of one each $10M$ of evolution. More precisely, the code limits the maximum refinement level to

$$\ell_{\max} \leq \begin{cases} 0 & \text{if } \text{rvu} < 100M \\ \left\lceil \frac{\text{rvu} - 100M}{10M} \right\rceil & \text{if } \text{rvu} \geq 100M \end{cases}, \quad (7)$$

where $\text{rvu} = \min(\text{rv}, \text{ru})$ is the distance from the closest point on the southeast or southwest grid faces.

6 Numerical Tests of the AMR Algorithm

As a test case for the slice-recursion AMR algorithm, I consider a particular example of the model problem of section 2, which arises in the course of calculating the radiation-reaction “self-force” on a scalar particle orbiting a Schwarzschild black hole (Barack and Ori (2002), see Barack (2009) for a general review). I take ϕ to be a complex scalar field, with the potential $V(r)$ and source term $S(t_{\text{Schw}})$ given by

$$V_\ell(r) = \frac{f(r)}{4} \left(\frac{2M}{r^3} + \frac{\ell(\ell+1)}{r^2} \right) \quad (8)$$

$$S_{\ell m}(t_{\text{Schw}}) = \frac{\pi q f^2(r_p) a_{\ell m}}{r_p E(r_p)} \exp(-im\omega(r_p)t_{\text{Schw}}), \quad (9)$$

where

$$\omega(r) = \sqrt{\frac{M}{r^3}} \quad (10)$$

and

$$E(r) = f(r) \left(1 - \frac{3M}{r} \right)^{-1/2}. \quad (11)$$

are respectively the orbital frequency and energy per unit mass of a particle in circular orbit at areal radius r in Schwarzschild spacetime. The coefficients $a_{\ell m}$ are defined such that the spherical harmonic $Y_{\ell m}(\theta=\frac{\pi}{2}, \varphi) = a_{\ell m} e^{im\varphi}$, i.e.,

$$a_{\ell m} = \begin{cases} (-1)^{(\ell+m)/2} \sqrt{\frac{2\ell+1}{4\pi}} \sqrt{\frac{(\ell+m-1)!! (\ell-m-1)!!}{(\ell+m)!! (\ell-m)!!}} & \text{if } \ell-m \text{ is even} \\ 0 & \text{if } \ell-m \text{ is odd} \end{cases}, \quad (12)$$

where the “double factorial” function is defined by

$$n!! = \begin{cases} n \cdot (n-2)!! & \text{if } n \geq 2 \\ 1 & \text{if } n \leq 1 \end{cases} . \quad (13)$$

For this test, I take $\ell = m = 10$, $r_p = 10M$, and use a problem domain size of $D = 200M$ on a side. Here $v_{\min} = 12.773M$, $u_{\min} = -12.773M$, and the grid extends from $rv = 0M$ to $rv = 200M$ and from $ru = 0M$ to $ru = 200M$.

The physical boundary data is zero along the southwest and southeast grid faces, and the extended initial data is computed using the 2-level subsampling scheme described in appendix A.2.4. The base grid has a resolution of $0.25M$, the finite differencing is the globally-4th-order scheme, and the error tolerance for the LTE estimate is 10^{-16} . As discussed in section 5.3.1, mesh refinement is suppressed for the first $100M$ of the evolution and the first $100M$ of each slice thereafter, and then turned on gradually at the rate of one refinement level for each further $10M$ of evolution.

Figure 6 shows a “map” of the mesh refinement, giving the highest refinement level at each event in the problem domain. Notice that the highest-refinement grids only cover small regions close to the particle worldline.

The online supplemental materials which accompany this paper include a movie (online resource 1) showing the spacetime-dependence of ϕ and the placement of the refined grids; figure 7 shows several sample frames and explains them in more detail.

Because of the adaptive placement of refined grids, it’s difficult to do a standard convergence test (Choptuik (1991)). Instead, I have followed Choptuik (1992) in adding an option

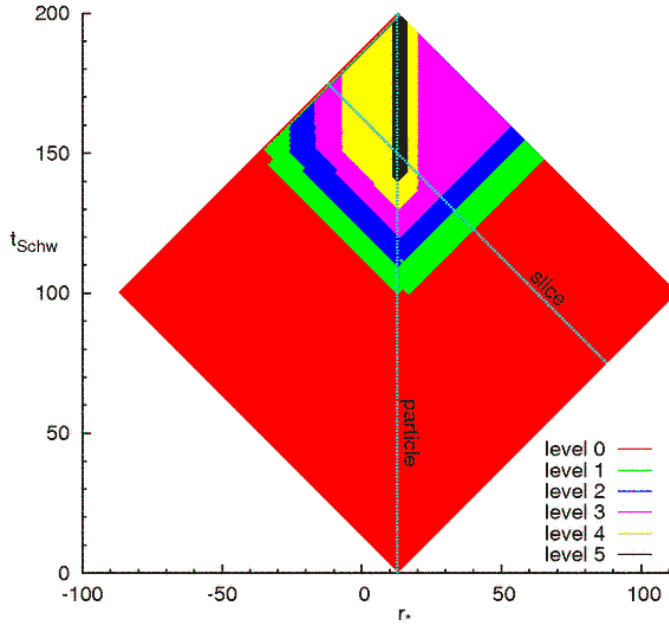


Fig. 6 This figure shows a “map” of the mesh refinement, giving the highest refinement level at each event in the problem domain. The vertical dashed line labelled “particle” shows the particle worldline. The diagonal dashed line labelled “slice” shows the $rv = 150M$ slice; figure 8 shows convergence tests on that slice.

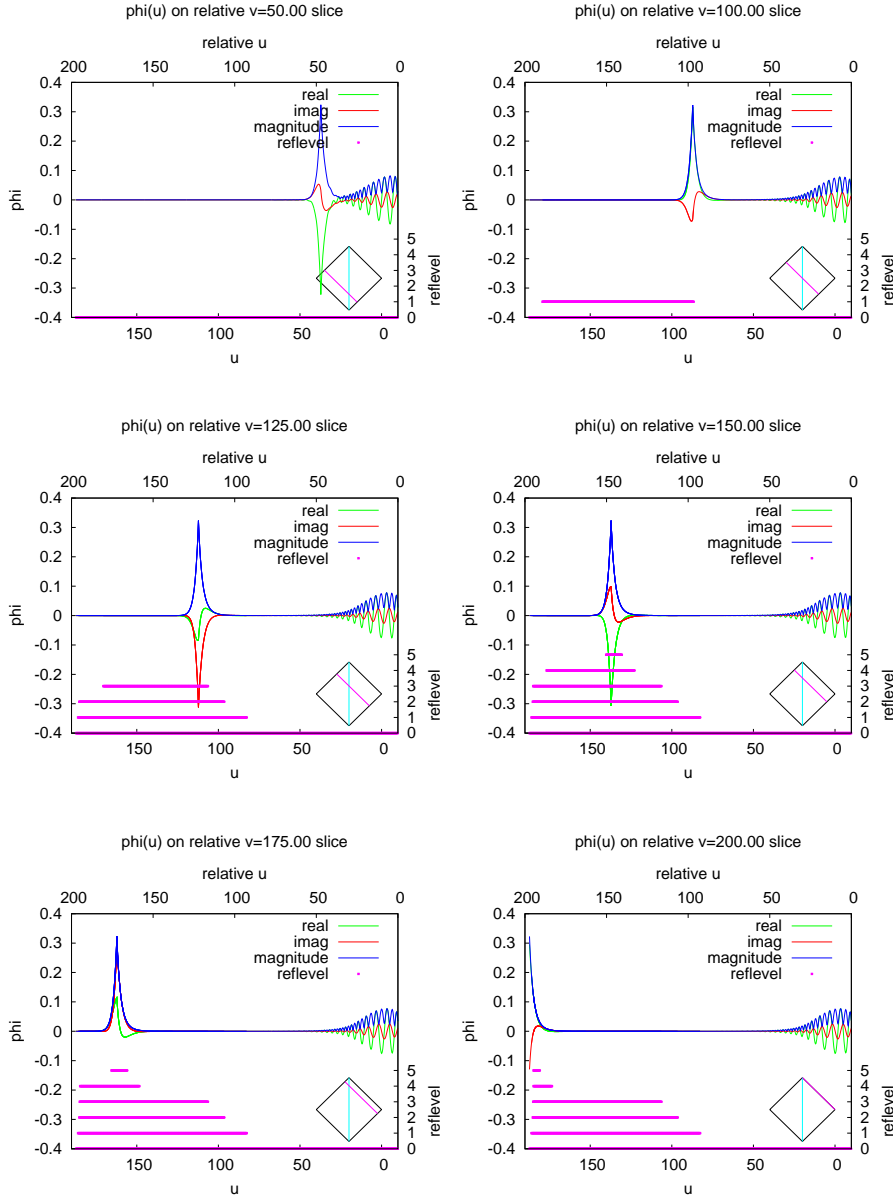


Fig. 7 This figure shows sample frames from the movie accompanying this paper (online resource 1). Each frame of the movie shows a single $rv = \text{constant}$ slice, and plots $\text{Re}[\phi]$, $\text{Im}[\phi]$, and $\|\phi\|$ on the left scale, and the spatial extent of each refinement level (on the right scale) as the horizontal lines. The u , ru , and rv coordinates are all shown in units of the Schwarzschild spacetime mass M . Each frame of the movie also includes a subplot (in the lower right corner) showing the location of that plot's $rv = \text{constant}$ slice within the entire problem domain. The vertical line in the subplot shows the particle worldline.

to my code to write out a “script” of the position and grid spacing of each grid generated by the AMR algorithm, and a related option to “play back” such a script. For a convergence test, I first run a “record” evolution, then generate a “playback $\times N$ ” script by refining each grid in the script by a chosen (small integer) factor N , and finally “play back” the refined script.

Figure 8 shows an example of such a convergence test for the field ϕ on the $rv = 150M$ slice. The code shows excellent 4th order convergence in the interior of each grid, across mesh-refinement boundaries, and near to the particle.

Profiling the code shows that almost all of the CPU time is consumed in the basic diamond-cell integration code, and the code’s overall running time is closely proportional to the number of diamond cells integrated. In other words, the AMR bookkeeping consumes only a negligible fraction of the CPU time.

For this evolution, the AMR evolution integrates a total of 35.6×10^6 diamond cells. Of these, 16% are accounted for by the re-integration of coarse slices after fine-grid recursion (lines 43–48 of figure 3). A hypothetical unigrid evolution covering the entire problem domain at the resolution of the finest AMR grid (level 5) would require integrating 655×10^6 diamond cells, 18.4 times as many as the AMR evolution. That is, for this problem the AMR evolution was approximately a factor of 18 faster than an equivalent-resolution (and thus equivalent-accuracy) unigrid evolution.

To further characterize the performance of the slice-recursion algorithm, I consider a sample of 295 separate evolutions of the same model problem, with each evolution having a different (ℓ, m) in the range $0 \leq \ell \leq 40$ and $0 \leq m \leq \ell$, and a problem-domain size between $400M$ and $30000M$.¹⁴ The globally-4th-order scheme is used for all of these evolutions, with an error tolerance for the LTE estimate of 10^{-16} . Figure 9 shows histograms of the re-integration overhead (the fraction of all diamond-cells integrations which occur as part of coarse-grid re-integrations) and the AMR speedup factor for this sample of evolutions. The re-integration overhead is usually between 20% and 25%, and never exceeds 30%.

For this sample the AMR speedup factor varies over a much wider range, from as low as 8.9 to as high as 400. The median speedup factor is 19, and 95% of the speedup factors are between 12 and 51.

7 Conclusions

The main result of this paper is that only a small modification (the tail re-integration, i.e., the lines marked with \bullet in figure 3) is needed to adapt the standard Cauchy Berger-Oliger AMR algorithm to characteristic coordinates and grids. The resulting “slice-recursion” algorithm uses relatively coarse-grained control for the recursion and the adaptivity part of AMR, which greatly simplifies the memory management, allowing entire null slices to be stored in contiguous arrays in memory. The algorithm can readily accomodate any order of finite differencing scheme; I present schemes for both 2nd and 4th order global truncation error.

The numerical tests results presented here demonstrate that the slice-recursion algorithm is highly efficient and displays excellent 4th order convergence. This algorithm readily accommodates a moving “particle” Dirac δ -function source term (which leads to a solution which is generically only C^1 at the particle position); there is no loss of convergence there.

¹⁴ This set of evolutions arises naturally as part of a calculation of the radiation-reaction “self-force” on a scalar particle orbiting a Schwarzschild black hole. Details of this calculation will be reported elsewhere; for present purposes these evolutions provide a useful set of test cases for the AMR algorithm.

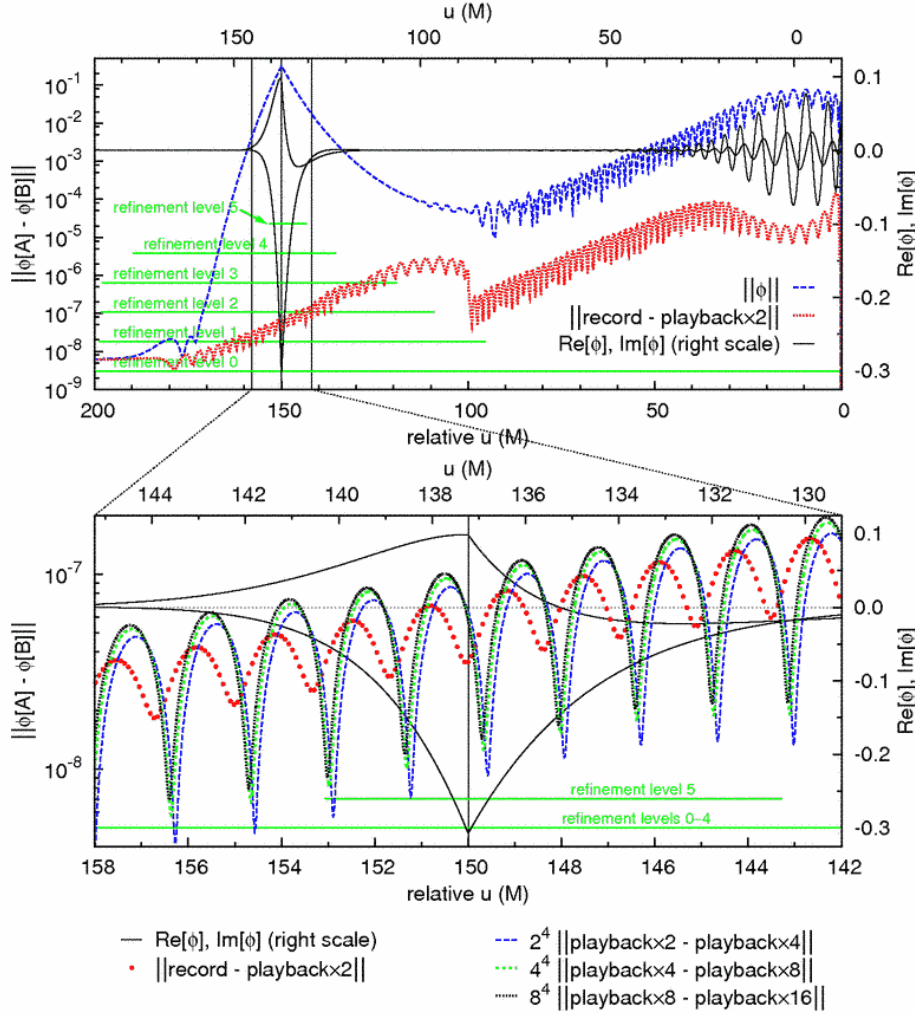


Fig. 8 This figure shows ϕ and its convergence on the $rv = 150M$ slice. In each subfigure, the solid vertical line at $ru = 150M$ shows the particle position. The upper subfigure (which shows the entire slice) plots the real and imaginary parts of ϕ on the right (linear) scale, and the complex norm $||\phi||$ on the left (logarithmic) scale. It also plots one of the convergence differences $||\text{record} - \text{playback} \times 2||$ on the left (logarithmic) scale. The horizontal lines show the portion of this slice covered by each refinement level. The lower subfigure (which shows an expanded view of a $\pm 8M$ region centered on the particle position) plots the real and imaginary parts of ϕ on the right (linear) scale, and the four convergence differences (scaled by the 4th power of the resolution) on the left (logarithmic) scale. Notice that the three higher-resolution scaled-convergence-difference curves are almost superimposed, indicating excellent 4th-order convergence, and that this convergence is not degraded either across the mesh-refinement boundaries at $rv = 143.3M$ and $rv = 153.1M$, or near the particle at $rv = 150M$.

The main potential disadvantage of the slice-recursion algorithm over the standard Cauchy Berger-Oliger algorithm is the cost of the tail re-integration. This cost depends on the placement of fine grids relative to their coarser parent grids; the worst possible case is a factor of 2 overhead in the coarse-grid part of the integration. There is no overhead for the finest level of the mesh-refinement hierarchy. In practice I find the re-integration cost to be quite modest, typically about 20–25% of the total computation, and (in my tests) never exceeding 30%. Compared to an equivalent-resolution unigrid evolution, I find that the slice-recursion algorithm is always much faster, with the exact speedup factor varying widely from one problem to another: for a sample of 295 test cases, 95% of the speedup factors are between 12 and 51.

The largest practical obstacle to the use of Berger-Oliger mesh refinement algorithms, including the slice-recursion algorithm presented here, is probably their implementation (programming) complexity. This is much less of an obstacle if codes can be shared across projects and researchers. To this end, my code implementing the slice-recursion algorithm is included in the electronic supplementary materials accompanying this paper (online resource 2), and is freely available to other researchers under the terms of the GNU general public license. This code uses C++ templates to support both 2nd and 4th order global truncation error, and both real and complex scalar fields, with no run-time overhead. It would be fairly easy to adapt the code to other finite differencing schemes and/or PDEs.

Pretorius and Lehner (2004, sections 4.2 and 4.3) describe how their characteristic Berger-Oliger algorithm can be extended to problems of higher dimensionality than 1+1 (i.e., problems whose domains have multiple spacelike dimensions), and how the algorithm may be parallelized. The techniques they describe should all apply equally to the slice-recursion algorithm presented here.

Acknowledgements I thank Leor Barack, Darren Golbourn, and Norichika Sago for introducing me to the self-force problem, and both they and Ian Hawke for many valuable conversations. I thank Virginia J. Vitzthum for useful comments on this manuscript. I thank the University of Southampton and the Max-Planck-Institut für Gravitationsphysik for their generous support during various stages of the research described in this manuscript.

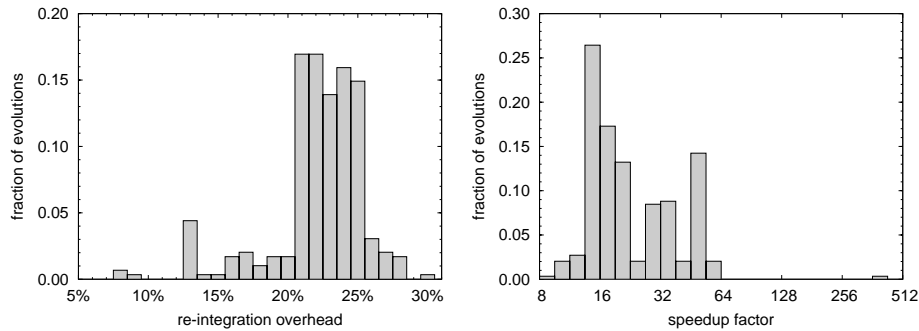


Fig. 9 This figure shows histograms of the re-integration overhead (the fraction of all diamond-cell integrations which occur as part of coarse-grid re-integrations, i.e., those in lines 43–48 of figure 3) and of the AMR speedup factor (the ratio of the number of cells that would have been integrated in hypothetical unigrid evolution covering the entire problem domain at the resolution of the finest AMR grid, to the number of cells actually integrated in the AMR evolution) for a sample of 295 evolutions. The re-integration overhead is usually between 20% and 25%, and never exceeds 30%, while the speedup factor varies much more widely.

References

- Anderson, M., E. W. Hirschmann, S. L. Liebling, and D. Neilsen, 2006, *Class. Quant. Grav.* **23**(22), 6503.
- Barack, L., 2009, *Class. Quant. Grav.* **26**(21), 213001.
- Barack, L., and A. Ori, 2002, *Phys. Rev. D* **66**(8), 084022.
- Berger, M. J., 1982, *Adaptive Mesh Refinement for Hyperbolic Partial Differential Equations*, Ph.D. thesis, Stanford University, University Microfilms #DA 83-01196.
- Berger, M. J., 1986, *SIAM Journal of Scientific and Statistical Computing* **7**(3), 904.
- Berger, M. J., and P. Colella, 1989, *J. Comput. Phys.* **82**(1), 64.
- Berger, M. J., and J. Oliger, 1984, *J. Comput. Phys.* **53**(3), 484.
- Brown, D. L., G. S. Chesshire, W. D. Henshaw, and D. J. Quinlan, 1999a, in *Eighth SIAM Conference on Parallel Processing for Scientific Computing, held in Minneapolis, Minnesota, 14–17 March 1997*, edited by M. T. Heath, V. Torczon, and G. Astfalk (SIAM), number 94 in *Proceedings in Applied Mathematics*, ISBN 978-0898713954.
- Brown, D. L., W. D. Henshaw, and D. J. Quinlan, 1999b, in *Object oriented methods for interoperable scientific and engineering: Proceedings of the SIAM Interdisciplinary Workshop on Object Oriented Methods for Interoperable Scientific and Engineering Computing, held in Yorktown Heights, New York, 21–23 October 1998*, edited by M. E. Henderson and S. L. Lyons (SIAM), number 99 in *Proceedings in Applied Mathematics*, pp. 245–255, ISBN 978-0898714456.
- Brügmann, B., 1996, *Phys. Rev. D* **54**(12), 7361.
- Brügmann, B., J. A. González, M. Hannam, S. Husa, U. Sperhake, and W. Tichy, 2008, *Phys. Rev. D* **77**(2), 024027.
- Brügmann, B., W. Tichy, and N. Jansen, 2004, *Phys. Rev. Lett.* **92**(21), 211101.
- Buchman, L. T., and O. C. A. Sarbach, 2006, *Class. Quant. Grav.* **23**(23), 6709.
- Buchman, L. T., and O. C. A. Sarbach, 2007, *Class. Quant. Grav.* **24**(12), S307.
- Burgarelli, D., M. Kischinhevsky, and R. J. Biezuner, 2006, *J. Comp. Appl. Math.* **196**(1), 115.
- Burko, L. M., and A. Ori, 1997, *Phys. Rev. D* **56**(12), 7820.
- Char, B., K. O. Geddes, W. M. Gentleman, and G. H. Gonnet, 1983, in *Lecture Notes in Computer Science 162: Computer Algebra*, edited by J. A. van Hulzen (Springer-Verlag), pp. 101–115.
- Choptuik, M. W., 1986, *A Study of Numerical Techniques for Radiative Problems in General Relativity*, Ph.D. thesis, University of British Columbia, Vancouver, Canada.
- Choptuik, M. W., 1989, in *Frontiers in Numerical Relativity*, edited by C. Evans, L. Finn, and D. Hobill (Cambridge University Press, Cambridge, England), pp. 206–221.
- Choptuik, M. W., 1991, *Phys. Rev. D* **44**(10), 3124.
- Choptuik, M. W., 1992, in *Approaches to Numerical Relativity*, edited by R. d’Inverno (Cambridge University Press, Cambridge), pp. 202–222.
- Choptuik, M. W., 1993, *Phys. Rev. Lett.* **70**(1), 9.
- Choptuik, M. W., 1994, ad: An implementation of the berger-oliger mesh refinement algorithm for the wave equation in spherical symmetry, URL <http://laplace.phas.ubc.ca/Members/matt/Doc/ad.ps>.
- Choptuik, M. W., E. W. Hirschmann, S. L. Liebling, and F. Pretorius, 2003a, *Class. Quant. Grav.* **20**(9), 1857.
- Choptuik, M. W., E. W. Hirschmann, S. L. Liebling, and F. Pretorius, 2003b, *Phys. Rev. D* **68**(4), 044007.
- Colella, P., D. T. Graves, N. D. Keen, T. J. Ligocki, D. F. Martin, P. W. McCorquodale, D. Modiano, P. O. Schwartz, T. D. Sternberg, and B. V. Straalen, 2009a, Chombo software package for AMR applications, URL <https://seesar.lbl.gov/anag/chombo/index.html>.
- Colella, P., D. T. Graves, N. D. Keen, T. J. Ligocki, D. F. Martin, P. W. McCorquodale, D. Modiano, P. O. Schwartz, T. D. Sternberg, and B. V. Straalen, 2009b, *Chombo Software Package for AMR Applications: Design Document*, Technical Report, Applied Numerical Algorithms Group, Computational Research Division, Lawrence Berkeley National Laboratory, URL <https://seesar.lbl.gov/anag/chombo/ChomboDesign-3.0.pdf>.
- Deiterding, R., 2005a, AMROC: Blockstructured adaptive mesh refinement in object-oriented C++, URL <http://amroc.sourceforge.net/index.htm>.
- Deiterding, R., 2005b, in *Adaptive Mesh Refinement - Theory and Applications: Proceedings of the Chicago Workshop on Adaptive Mesh Refinement Methods, held Sept. 3–5, 2003* (Springer-Verlag, Berlin), volume 41 of *Lecture Notes in Computational Science and Engineering*, pp. 361–372.
- Deiterding, R., 2006, *Int. J. Comp. Sci. and Eng.* **1**(1/2/3), 64.
- Dursi, L. J., and M. Zingale, 2003, *astro-ph/0310891*.
- Givoli, D., 1991, *J. Comp. Phys.* **94**(1), 1.
- Gómez, R., and J. Winicour, 1992, *J. Math. Physics* **33**(4), 1445.
- Gómez, R., J. Winicour, and R. Isaacson, 1992, *J. Comp. Phys.* **98**(1), 11.

- Goodale, T., G. Allen, G. Lanfermann, J. Massó, T. Radke, E. Seidel, and J. Shalf, 2003, in *Vector and Parallel Processing – VECPAR’2002, 5th International Conference, Lecture Notes in Computer Science* (Springer, Berlin).
- Goodale, T., J. Massó, G. Allen, G. Lanfermann, and J. Shalf, 1999, The Cactus code, URL <http://www.cactuscode.org>.
- Gundlach, C., R. Price, and J. Pullin, 1994, Phys. Rev. D **49**(2), 883.
- Haas, R., 2007, Phys. Rev. D **75**(12), 124011.
- Hamadé, R. S., and J. M. Stewart, 1996, Class. Quant. Grav. **13**(3), 497.
- Henshaw, W. D., D. L. Brown, G. S. Chesshire, and D. J. Quinlan, 2002, The Overture code, URL <http://acts.nersc.gov/overture/>.
- Hornung, R. D., and S. R. Kohn, 1999, in *Object oriented methods for interoperable scientific and engineering: Proceedings of the SIAM Interdisciplinary Workshop on Object Oriented Methods for Interoperable Scientific and Engineering Computing, held in Yorktown Heights, New York, 21–23 October 1998*, edited by M. E. Henderson and S. L. Lyons (SIAM), number 99 in Proceedings in Applied Mathematics, pp. 235–244, ISBN 978-0898714456.
- Hornung, R. D., and S. R. Kohn, 2002a, Concurrency and Computation: Practice and Experience **14**(5), 347.
- Hornung, R. D., and S. R. Kohn, 2002b, SAMRAI: Structured Adaptive Mesh Refinement Application Infrastructure, URL <https://computation.llnl.gov/casc/SAMRAI/index.html>.
- Hornung, R. D., A. M. Wissink, and S. R. Kohn, 2006, Engineering with Computers **22**(3–4), 181.
- Husa, S., J. A. González, M. Hannam, B. Brügmann, and U. Sperhake, 2008, Class. Quant. Grav. **25**(10), 105006.
- Kidder, L. E., L. Lindblom, M. A. Scheel, L. T. Buchman, and H. P. Pfeiffer, 2005, Phys. Rev. D **71**(6), 064020.
- Kreiss, H. O., and J. Oliger, 1973, *Methods for the approximate solution of time dependent problems* (GARP publication series No. 10, Geneva).
- Lea, D., 2000, A memory allocator, web page last modified 4 April 2000, accessed on 24 August 2009, URL <http://gee.cs.oswego.edu/dl/html/malloc.html>.
- Lehner, L., S. L. Liebling, and O. Reula, 2006, Class. Quantum Grav. **23**(16), S421.
- LeVeque, R. J., 2002, *Finite Volume Methods for Hyperbolic Problems* (Cambridge University Press, Cambridge, U.K.), ISBN 0-521-00924-3.
- LeVeque, R. J., 2007, *Finite Difference Methods for Ordinary and Partial Differential Equations* (SIAM Press, Philadelphia, USA), ISBN 978-0-898716-29-0.
- Liebling, S. L., 2002, Phys. Rev. D **66**(4), 041703.
- Liebling, S. L., 2004, Class. Quant. Grav. **21**(16), 3995.
- Lijewski, M., V. E. Beckner, and C. A. Rendleman, 2006, CCSE software infrastructure: BoxLib and AmrLib, URL <http://seesar.lbl.gov/ccse/Software/index.html>.
- Lousto, C. O., 2005, Class. Quant. Grav. **22**(15), S543.
- Lousto, C. O., and R. H. Price, 1997, Phys. Rev. D **56**(10), 6439.
- MacNeice, P., K. M. Olson, C. Mobarry, R. de Fainchtein, and C. Packer, 2000, Comp. Phys. Comm. **126**(3), 330.
- Martel, K., and E. Poisson, 2002, Phys. Rev. D **66**(8), 084001.
- Mitra, S., M. Parashar, and J. Browne, 1995, DAGH: User’s guide, URL <http://userweb.cs.utexas.edu/users/dagh/>.
- Olson, K. M., 2006, in *Parallel Computational Fluid Dynamics 2005: Theory and Applications: Proceedings of the Parallel CFD Conference, College Park, MD, USA*, edited by A. Deane, A. Ecer, G. Brenner, D. Emerson, J. McDonough, J. Periaux, N. Satofuka, and D. Tromeur-Dervout (Elsevier).
- Olson, K. M., and P. MacNeice, 1999, Paramesh: Parallel adaptive mesh refinement, URL http://www.physics.drexel.edu/~olson/paramesh-doc/Users_manual/amr.html.
- Olson, K. M., and P. MacNeice, 2005, in *Adaptive Mesh Refinement - Theory and Applications: Proceedings of the Chicago Workshop on Adaptive Mesh Refinement Methods, Sept. 3-5, 2003*, edited by T. Plewa, T. Linde, and G. V. Weirs (Springer-Verlag, Berlin), volume 41 of *Lecture Notes in Computational Science and Engineering*.
- Parashar, M., and J. C. Browne, 2000, *IMA Volume on Structured Adaptive Mesh Refinement (SAMR) Grid Methods* (Springer-Verlag), chapter System Engineering for High Performance Computing Software: The HDDA/DAGH Infrastructure for Implementation of Parallel Structured Adaptive Mesh Refinement, pp. 1–18.
- Parashar, M., and X. Li, 2009, in *Advanced Computational Infrastructures for Parallel and Distributed Applications*, edited by M. Parashar, X. Li, and S. Chandra (Wiley, New York), ISBN 978-0-470-07294-3, pp. 249–263.

- Pretorius, F., 2002a, AMRD reference manual, URL http://laplace.phas.ubc.ca/Doc/pamr/AMRD_ref.pdf.
- Pretorius, F., 2002b, *Numerical Simulations of Gravitational Collapse*, Ph.D. thesis, University of British Columbia, Vancouver, Canada.
- Pretorius, F., 2002c, PAMR reference manual, URL http://laplace.phas.ubc.ca/Doc/pamr/PAMR_ref.pdf.
- Pretorius, F., and M. Choptuik, 2006, J. Comput. Phys. **218**(1), 246.
- Pretorius, F., and L. Lehner, 2004, J. Comput. Phys. **198**(1), 10.
- Rendleman, C. A., V. E. Beckner, M. Lijewski, W. Crutchfield, and J. B. Bell, 2000, Computing and Visualization in Science **3**, 147.
- Richtmyer, R. D., and K. Morton, 1994, *Difference Methods for Initial Value Problems* (Kreiger, Malabar, Florida, USA), 2nd edition, ISBN 0-89464-763-6.
- Rinne, O., 2006, Class. Quant. Grav. **23**(22), 6275.
- Rinne, O., L. T. Buchman, M. A. Scheel, and H. P. Pfeiffer, 2009, Class. Quant. Grav. **26**(7), 075009.
- Rinne, O., L. Lindblom, and M. A. Scheel, 2007, Class. Quant. Grav. **24**(16), 4053.
- Ruiz, M., O. Rinne, and O. Sarbach, 2007, Class. Quant. Grav. **24**(24), 6349.
- Schnetter, E., 2001, CARPET: A mesh refinement driver for CACTUS, URL <http://www.carpetcode.org>.
- Schnetter, E., S. H. Hawley, and I. Hawke, 2004, Class. Quantum Grav. **21**(6), 1465.
- Seiler, J., B. Szilágyi, D. Pollney, and L. Rezzolla, 2008, Class. Quant. Grav. **25**(17), 175020.
- Su, J. Z., T. Wen, and K. A. Yelick, 2006, *Compiler and Runtime Support for Scaling Adaptive Mesh Refinement Computations in Titanium*, Technical Report UCB/EECS-2006-87, Electrical Engineering and Computer Sciences Department, University of California at Berkeley, URL <http://www.eecs.berkeley.edu/Pubs/TechRpts/2006/EECS-2006-87.pdf>.
- Tornberg, A.-K., and B. Engquist, 2004, J. Comp. Phys. **200**(2), 462.
- Wald, R. M., 1984, *General relativity* (The University of Chicago Press, Chicago), ISBN 0-226-87032-4 (hardcover), 0-226-87033-2 (paperback).
- Welling, J. S., 1983, *Numerical calculations in the characteristic initial value problem in general relativity*, Ph.D. thesis, University of Pittsburgh, Pittsburgh, university Microfilms Order #84-11,762.
- Wilson, P. R., M. S. Johnstone, M. Neely, and D. Boles, 1995, in *Proceedings of the 1995 International Workshop on Memory Management*, edited by H. G. Baker (Springer-Verlag), volume 986 of *Lecture Notes in Computer Science*, chapter Dynamic Storage Allocation: A Survey and Critical Review, ISBN 978-3540603689, pp. 1–116.
- Winicour, J., 2009, Living Reviews in Relativity **12**(3), URL <http://www.livingreviews.org/lrr-2009-3>.

A Details of the Unigrid Finite Differencing Scheme

In this appendix, I describe the finite differencing schemes in detail for the model problem (3), for both 2nd and 4th order GTE.

In this appendix only, when describing the computation of ϕ at a particular grid point (j, i) , I sometimes use an abbreviated notation for grid-point indexing, denoting the grid point $(j - n, i - m)$ by a subscript nm . Such subscripts can be distinguished from the usual grid-point indices by the absence of a comma between the two indices. These abbreviated subscripts may be either integral or half-integral, and in this latter context (only) I also use the abbreviation $h \equiv \frac{1}{2}$. For example, ϕ_{12} denotes $\phi_{j-1, i-2}$, while ϕ_{0h} denotes $\phi_{j, i-1/2}$.

A.1 Second Order Global Accuracy

To discretize the wave equation (3) to 2nd order global accuracy in the grid spacing Δ , I use a standard diamond-cell integration scheme (Gómez and Winicour (1992); Gómez *et al.* (1992); Gundlach *et al.* (1994); Burko and Ori (1997); Lousto and Price (1997); Lousto (2005); Winicour (2009)): Consider a double-null “diamond” grid cell of side Δ , with “north”, “west”, “east”, and “south” vertices (grid points) N, W, E, and S respectively, and central point C, as shown in figure 10.

Consider first the vacuum case, where the particle worldline $r = r_p$ doesn’t intersect the cell and hence the right hand side of the wave equation (3) vanishes everywhere in the cell. Integrating this equation over the cell then gives

$$\left(\phi_N + \phi_S - \phi_E - \phi_W\right) + \left(\Delta^2 V_C \frac{\phi_E + \phi_W}{2} + \mathcal{O}(\Delta^4)\right) = 0, \quad (14)$$

or equivalently

$$\phi_N = \phi_E + \phi_W - \phi_S - \Delta^2 V_C \frac{\phi_E + \phi_W}{2} + \mathcal{O}(\Delta^4), \quad (15a)$$

where subscripts denote the value of the field at the corresponding grid point.

If the particle worldline $r = r_p$ intersects the cell, then as discussed in section 3, I assume it does so symmetrically. Integrating the right-hand-side source term in (3) over the grid cell then adds an extra term

$$\int_{\text{cell}} S(t_{\text{Schw}}) \delta(r - r_p) dv du = \frac{2}{f(r_p)} \int_{t_C - \Delta/2}^{t_C + \Delta/2} S(t_{\text{Schw}}) dt_{\text{Schw}} \quad (15b)$$

to the right hand side of (15a), where $t_C \equiv (t_{\text{Schw}})_C$. For the test case considered in section 6, this source-term integral becomes

$$\frac{2}{f(r_p)} \int_{t_C - \Delta/2}^{t_C + \Delta/2} S_{\ell m}(t_{\text{Schw}}) dt_{\text{Schw}} = \frac{2\pi q f(r_p) a_{\ell m}}{r_p E(r_p)} \exp(-im\omega(r_p)t_C) \Delta \text{sinc}\left(\frac{1}{2}m\omega(r_p)\Delta\right) + \mathcal{O}(\Delta^3). \quad (16)$$

A.2 Fourth Order Global Accuracy

To discretize the wave equation (3) to 4th order global accuracy in the grid spacing Δ , I use a scheme based on that of Haas (2007) (see also Lousto (2005)), but modified in its treatment of cells near the particle. The modification makes the scheme fully explicit, removing the need for an iterative computation at each cell intersecting the particle. However, the scheme is only valid with the assumption noted above, that if the particle intersects a cell it does so symmetrically. In practice (cf. footnote 2), this means that the scheme is only valid for the case where r_p is constant, i.e., the particle is in a circular orbit around the central black hole.

Consider the computation of $\phi_{j,i}$, and suppose the particle worldline intersects the $v = v_j$ slice at the grid point $i = i_p$. There are several different cases for the finite differencing scheme, depending on the sign and magnitude of $i - i_p$. Figure 10 shows all of these cases.

A.2.1 $|i - i_p| \geq 3$ (Cell far from the particle)

If $|i - i_p| \geq 3$ (so that the particle worldline doesn't intersect any part of the finite difference molecule), then I use the finite differencing scheme of Haas's equations (2.7), (2.10), and (4.10). That is (following Lousto (2005) and Haas (2007)) I first define the new grid function $G \equiv V\phi$. I then interpolate G_{hh} via Haas's equation (2.7), which in my notation reads

$$G_{hh} = \frac{1}{16} \left[(8G_{10} + 8G_{01}) + (-4G_{20} + 8G_{11} - 4G_{02}) + (G_{30} - G_{21} - G_{12} + G_{03}) \right] + \mathcal{O}(\Delta^3). \quad (17)$$

I then compute $G_\Sigma \equiv G_{h0} + G_{0h} + G_{1h} + G_{h1}$ via Haas's equation (2.10), which in my notation reads

$$\begin{aligned} G_\Sigma &= 2 \left(1 - \frac{1}{2} \Delta_2^2 V_{hh} \right) G_{hh} \\ &\quad + \left(1 - \frac{1}{2} \Delta_2^2 V_{h0} \right) V_{h0} \phi_{10} + \left(1 - \frac{1}{2} \Delta_2^2 V_{0h} \right) V_{0h} \phi_{01} \\ &\quad + \frac{1}{2} \left(V_{h0} - 2V_{hh} + V_{0h} \right) (\phi_{10} + \phi_{01}), \end{aligned} \quad (18)$$

where $\Delta_2 \equiv \Delta/2$.

Finally, I compute ϕ_{00} via Haas's equation (4.7), which in my notation reads

$$\begin{aligned} \phi_{00} &= -\phi_{11} \\ &\quad + \left[1 - \left(\frac{1}{4} \Delta_3^2 - \frac{1}{16} \Delta_3^4 V_{hh} \right) (V_{hh} + V_{10}) \right] \phi_{10} \\ &\quad + \left[1 - \left(\frac{1}{4} \Delta_3^2 - \frac{1}{16} \Delta_3^4 V_{hh} \right) (V_{hh} + V_{01}) \right] \phi_{01} \\ &\quad - \left[\left(1 - \frac{1}{4} \Delta_3^2 V_{hh} \right) \Delta_3^2 \right] (G_\Sigma + 4G_{hh}), \end{aligned} \quad (19)$$

where $\Delta_3 \equiv \Delta/3$.

A.2.2 $i = i_p \pm 1$ or $i = i_p \pm 2$ (Cell near the particle)

If $i - i_p = -1$ or -2 (so we are computing ϕ at a grid point near to, but to the right of, the particle), then the interpolation (17) would use data from both sides of the particle's worldline (hereinafter I refer to this as "crossing" the worldline), violating the smoothness assumptions used in the interpolation's derivation. Instead, I use the "right" interpolation

$$G_{hh} = \frac{3}{8}G_{10} + \frac{5}{8}G_{01} + \frac{1}{4}G_{11} - \frac{1}{4}G_{02} - \frac{1}{8}G_{21} + \frac{1}{8}G_{12} + \mathcal{O}(\Delta^3), \quad (20)$$

which (since $i < i_p$) doesn't cross the worldline.

If $i - i_p = +1$ or $+2$ (so we are computing ϕ at a grid point near to, but to the left of, the particle), then again the interpolation (17) would cross the particle's worldline, so I instead use the "left" interpolation

$$G_{hh} = \frac{3}{8}G_{01} + \frac{5}{8}G_{10} + \frac{1}{4}G_{11} - \frac{1}{4}G_{20} - \frac{1}{8}G_{12} + \frac{1}{8}G_{21} + \mathcal{O}(\Delta^3), \quad (21)$$

which (since $i > i_p$) doesn't cross the worldline.

[Each of the interpolations (17), (20), and (21) is actually valid for any grid function which is smooth (has a convergent Taylor series in v and u) throughout the region spanned by the interpolation molecule.]

Once G_{hh} has been computed, G_Σ and then G_{00} can be computed in the same manner as before, i.e., via (18) and (19) respectively.¹⁵

A.2.3 $i = i_p$ (Cell symmetrically bisected by the particle)

If $i = i_p$, then for each $k \in \{1, 2, 3\}$ I first compute an estimate $\phi_{j,i}^{(k)}$ for $\phi_{j,i}$ using the globally-2nd-order scheme (15) applied to the diamond cell of size $k\Delta$ defined by the four grid points $\mathbf{N}^{(k)} = (j, i)$, $\mathbf{W}^{(k)} = (j - k, i)$, $\mathbf{E}^{(k)} = (j, i - k)$, and $\mathbf{S}^{(k)} = (j - k, i - k)$. I then assume a Richardson expansion for $\phi^{(k)}(v, u)$ in the effective grid spacing $k\Delta$ (Choptuik (1991)),

$$\phi^{(k)}(v, u) = \phi(v, u) + (k\Delta)^3 P(v, u) + (k\Delta)^4 Q(v, u) + \mathcal{O}(\Delta^5), \quad (22)$$

where P and Q are smooth functions which do not depend on the grid spacing, and where the $\mathcal{O}(k\Delta^3)$ leading-order error term is that of (15b). Finally, I Richardson-extrapolate the value of $\phi_{j,i} \equiv \phi(v, u)$ from the three estimates $\phi_{j,i}^{(k)}$ to obtain

$$\phi_{j,i} = \frac{108}{85}\phi_{j,i}^{(1)} - \frac{27}{85}\phi_{j,i}^{(2)} + \frac{4}{85}\phi_{j,i}^{(3)} + \mathcal{O}(\Delta^5). \quad (23)$$

There are only $\mathcal{O}(N)$ $i = i_p$ cells, so this $\mathcal{O}(\Delta^5)$ LTE suffices to keep these cells' collective contribution to the global error at $\mathcal{O}(\Delta^4)$.

A.2.4 Initial Data

As shown in figure 10, the globally-4th-order finite difference molecules for computing $\phi_{j,i}$ generally include points on the $j-1$, $j-2$, and $j-3$ slices, and at the $i-1$, $i-2$, and $i-3$ u positions. This means that starting the integration on any grid requires "extended initial data" on 3 slices and on 3 points on each succeeding slice. This poses a problem for setting up the base grid at the very beginning of the integration,¹⁶ since physical boundary data is only specified along the southwest and southeast faces of the problem domain, i.e., on a single initial slice and at a single initial grid point of each succeeding slice.

There are several possible ways of obtaining the extended initial data:

Replication of the Physical Boundary Data For the self-force problem (Barack and Ori (2002)) the precise choice of boundary data doesn't matter, and it's acceptable to approximate the PDEs to a lower order of accuracy near the boundary. Thus for this use, the physical boundary data (in this case $\phi = 0$) can simply be replicated throughout the extended-initial-data region.

¹⁵ Notice that once G_{hh} is known, (18) and (19) use only the grid-function values ϕ_{10} , ϕ_{01} , and ϕ_{11} , and thus require only that the particle worldline doesn't pass between these points; this condition is satisfied whenever $i \neq i_p$.

¹⁶ There's no problem in starting the integration of other grids, since the extended initial data for any $\mathbf{G}^{(\ell)}$ with $\ell > 0$ is interpolated from its parent grid $\mathbf{G}^{(\ell-1)}$ (line 20 of figure 4).

Taylor-series Approximation For more general purposes, it's usually desirable to approximate the PDE to full accuracy everywhere in the problem domain, i.e., to compute the extended initial data to $\mathcal{O}(\Delta^4)$ accuracy. Lousto (2005, section 4.1) describes a Taylor-series approximation scheme to do this.

Two-Level Subsampling Another scheme for computing extended initial data is to define an auxiliary “subsampling” grid with spacing $\Delta_{ss} \ll \Delta$, which only covers the extended-initial-data region. Choose Δ_{ss} such that it integrally divides Δ and such that $\Delta_{ss} \propto \Delta^2$ for sufficiently high resolution. The extended initial data can now be computed by integrating the auxiliary grid using the globally-2nd-order scheme, then subsampling data from the auxiliary grid to the main grid. Because $\Delta_{ss} \propto \Delta^2$ at sufficiently high resolution, $\mathcal{O}(\Delta_{ss}^2) = \mathcal{O}(\Delta^4)$, i.e., the global accuracy remains 4th order with respect to the main-grid resolution Δ .

The auxiliary grid only needs to cover the first 3 slices of the main grid, together with the first 3 grid points of each later main-grid slice. However, this corresponds to $\mathcal{O}(1/\Delta)$ auxiliary-grid spacings, so integrating all the auxiliary-grid points requires $\mathcal{O}(1/\Delta^3)$ CPU time and $\mathcal{O}(1/\Delta^2)$ memory. This is much more expensive than the main-grid computation, which only requires $\mathcal{O}(1/\Delta^2)$ CPU time and $\mathcal{O}(1/\Delta)$ memory.

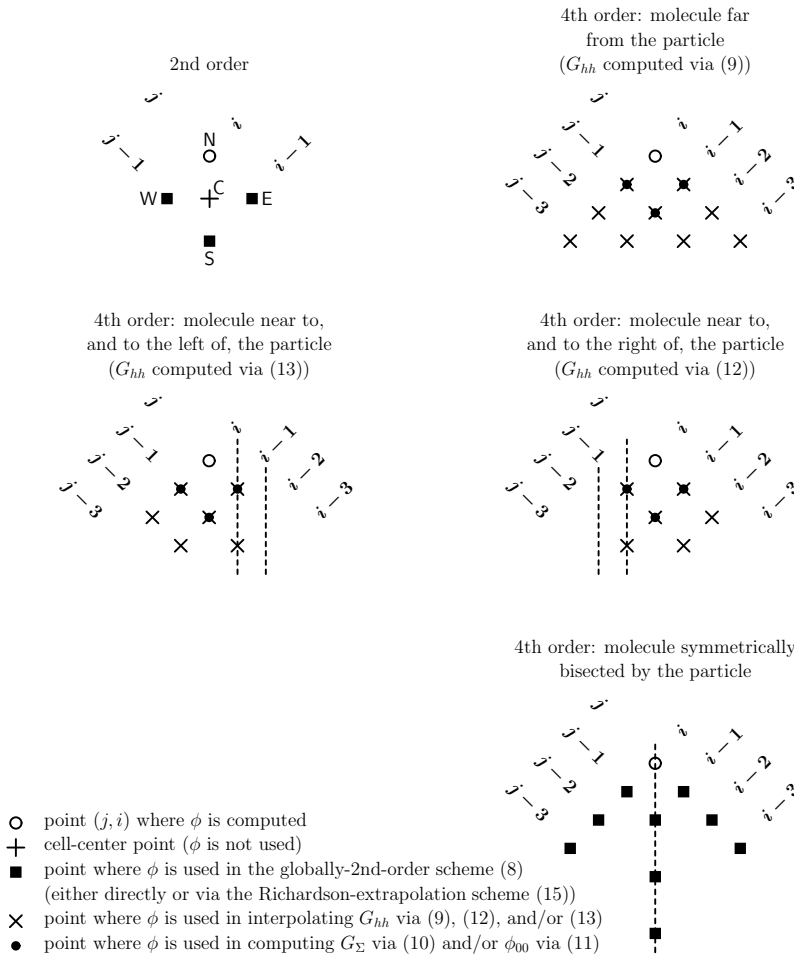
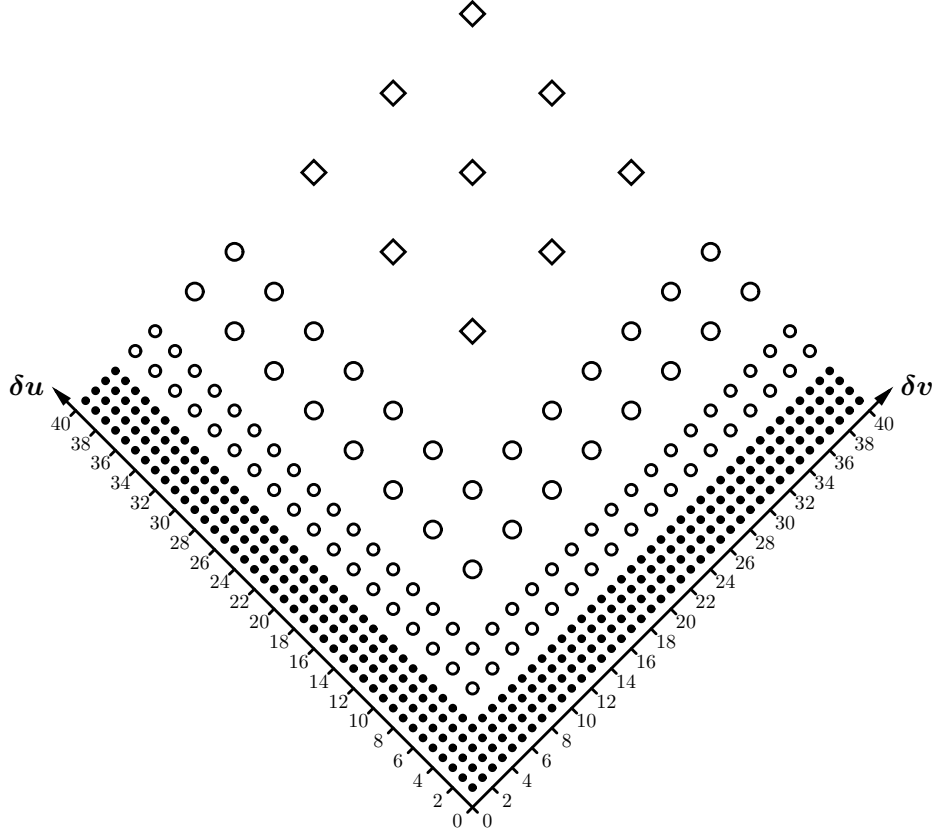


Fig. 10 This figure shows the unigrid finite differencing molecules. For clarity, the 2nd order molecule is enlarged relative to the 4th order molecules. In the lower 3 subfigures the vertical dashed lines show possible positions for the particle worldline.

Recursive Doubling A more efficient approach is to use a recursive-doubling scheme. Here we use a sequence of q auxiliary grids $A^{(0)}, A^{(1)}, A^{(2)}, \dots, A^{(q-1)}$, with $A^{(k)}$ having spacing $2^{k-q}\Delta$. We choose q such that $2^{-q}\Delta \leq \Delta_* < 2^{1-q}\Delta$ for some $\Delta_* \propto \Delta^2$ for sufficiently high resolution. The extended initial data for the main grid can now be computed as follows (see figure 11 for an example): First integrate $A^{(0)}$ using the globally-2nd-order scheme for 4 slices, and for 4 points on each succeeding slice. Then for each $k = 1, 2, 3, \dots, q-1$, subsample from $A^{(k-1)}$ to obtain the extended initial data to integrate $A^{(k)}$ using the globally-4th-order scheme for 2 slices, and for 2 points on each succeeding slice. Finally, subsample from $A^{(q-1)}$ to obtain the extended initial data to integrate the main grid using the globally-4th-order scheme.



- point in auxiliary grid $A^{(0)}$ (spacing 1) computed using globally-2nd-order scheme
- point in auxiliary grid $A^{(1)}$ (spacing 2) computed using globally-4th-order scheme (extended initial data subsampled from auxiliary grid $A^{(0)}$)
- point in auxiliary grid $A^{(2)}$ (spacing 4) computed using globally-4th-order scheme (extended initial data subsampled from auxiliary grid $A^{(1)}$)
- ◇ point in main grid (spacing 8) computed using globally-4th-order scheme (extended initial data subsampled from auxiliary grid $A^{(2)}$)

Fig. 11 This figure shows an example of the recursive-doubling technique for constructing extended initial data for the globally-4th-order initial data scheme. The grid axes are plotted in terms of $\delta u = u - u_{\min}$ and $\delta v = v - v_{\min}$, and the grid spacings are in units of finest ($\Delta_{\text{rd}}^{(0)}$) auxiliary grid spacing. In this example $q = 3$ auxiliary grids are used.

Each auxiliary grid only has to cover 2 or 4 slices, and 2 or 4 points on each succeeding slice, so this scheme is much more efficient than the two-level subsampling scheme: in the high-resolution limit the total cost of all the auxiliary-grid integrations is $\mathcal{O}(1/\Delta^2)$ CPU time, the same order as the main-grid computation. Unfortunately, even with careful memory management (discarding grid points as soon as they're no longer needed) the auxiliary grids still require $\mathcal{O}(1/\Delta^2)$ memory, much more than the main-grid computation's $\mathcal{O}(1/\Delta)$ memory requirement.

It's relatively easy to implement the recursive-doubling scheme in a code using the type of fine-grained linked-list data structures described by Pretorius and Lehner (2004), where the integration can “flow” in either the v direction or the u direction at any stage in the computation. However, for the slice-recursion algorithm we typically require that the integration proceed sequentially in the v direction and that any data reuse or subsampling take place within the small (typically 4–7) number of slices kept in memory at each refinement level. The recursive-doubling initial-data scheme thus requires interleaving the integration of the different auxiliary grids along the southeast face of the grid. Figure 12 gives a pseudocode outline of an algorithm to generate the appropriate sequence of integrations, subsamplings, and other grid operations for the recursive-doubling scheme.

A.3 The Coarse-Grid Instability

The finite differencing schemes discussed here become unstable at very low resolutions, in a manner somewhat resembling the classic Courant-Friedrichs-Lewy instability of Cauchy finite differencing. I have not mathematically analyzed this instability,¹⁷ but empirically it only occurs for very low resolutions (large Δ), with the instability threshold (the smallest Δ for which the instability appears) depending on ℓ , but not on m . Figure 13 shows the ℓ and Δ for which the instability occurs. Notice that the instability threshold decreases gradually with ℓ , and is somewhat smaller for the globally-4th-order scheme than for the globally-2nd-order scheme.

In practice, it's rare for this “coarse-grid instability” to be a significant problem because reasonable accuracy requirements normally force much higher resolutions than those where the instability would occur. The one exception to this is the base grid, which might otherwise be made very coarse (allowing the AMR to refine it as needed); the coarse-grid instability prevents this by requiring the base grid to be finer than the instability threshold.

B Implementation Details

B.1 Computing $r(r_*)$

The finite differencing schemes discussed here use finite-difference grids which are locally uniform in v and u , so it's trivial to compute the r_* coordinate of any grid point. However, the coefficients in the wave equation (3) are all given as explicit functions of r , so the code needs to know the r coordinate of each grid point (and, for the globally-4th-order scheme, also of the center of each grid zone). My code computes this as follows: Define

$$y \equiv \ln\left(\frac{r}{2M} - 1\right) \quad (24a)$$

$$x_* \equiv \frac{r_*}{2M}, \quad (24b)$$

so that $r = 2M(1 + e^y)$ and the definition (2) becomes $x_* = 1 + y + e^y$. Then $y(x_*)$ (and hence $r(r_*)$) can be found by using Newton's method to find a zero of the function

$$h(y) = 1 + y + e^y - x_* \quad (25)$$

An initial guess for Newton's method can be obtained by neglecting either y or e^y in (25), giving

$$y_{\text{initial guess}} = \begin{cases} \log(x_* - 1) & \text{if } x_* > 1 \text{ } (y \gtrsim -0.577) \\ x_* - 1 & \text{if } x_* \leq 1 \text{ } (y \lesssim -0.577) \end{cases} \quad (26)$$

¹⁷ Gómez and Winicour (1992); Gómez *et al.* (1992) discuss the stability of diamond-cell integration schemes in spherical symmetry; Welling (1983); Winicour (2009, section 3.3) discuss subtleties in applying the CFL condition to a more general null-cone evolution algorithm in axisymmetry.

```

1  global integer  $\ell_{\max}$       # maximum  $\ell$  for which we have created  $A^{(\ell)}$ 
2
3  procedure recursive_doubling_initial_data(integer q)
4  {
5    call create_grid(0)
6
7    for integer j from 1 to  $j_{\max}$ 
8    {
9      if ( $j = 5 \cdot 2^{\ell_{\max}}$ )
10     then  $A^{(\ell_{\max})}.i_{\max} \leftarrow 4 \cdot 2^{\ell_{\max}}$     # discard  $A^{(\ell_{\max})}$  grid points which are no longer needed
11     if ( $(\ell_{\max} < q)$  and ( $j = 6 \cdot 2^{\ell_{\max}}$ ))
12     then call create_grid( $\ell_{\max}+1$ )
13
14     for integer  $\ell$  from 0 to  $\ell_{\max}$ 
15     {
16       if ( $j \bmod 2^{\ell} = 0$ )
17       then call integrate_slice( $\ell, j$ )
18     }
19   }
20 }
21
22 # create the auxiliary grid  $A^{(\ell)}$  and update  $\ell_{\max}$ 
23 procedure create_grid(integer  $\ell$ )
24 {
25   Create the auxiliary grid  $A^{(\ell)}$  with spacing  $\delta = 2^{\ell}$  and size  $A^{(\ell)}.i_{\max}$  = the size of the main grid
26    $A_0^{(\ell)} \leftarrow$  physical boundary data on the southwest grid face
27   if ( $\ell > 0$ )
28   then {
29      $A_{\delta}^{(\ell)} \leftarrow$  subsample from  $A^{(\ell-1)}$ 
30      $A_{2\delta}^{(\ell)} \leftarrow$  subsample from  $A^{(\ell-1)}$ 
31   }
32    $\ell_{\max} \leftarrow \ell$ 
33 }
34
35 # integrate the auxiliary grid  $A^{(\ell)}$  on the slice j
36 procedure integrate_slice(integer  $\ell$ , integer j)
37 {
38    $A_{j,0}^{(\ell)} \leftarrow$  physical boundary data on the southeast grid face
39   if ( $\ell = 0$ )
40   then {
41     for integer i from 1 to  $A^{(0)}.i_{\max}$ 
42     {
43        $A_{j,i}^{(\ell)} \leftarrow$  update using the globally-2nd-order scheme
44     }
45   }
46   else {
47     integer  $\delta \leftarrow 2^{\ell}$ 
48      $A_{j,\delta}^{(\ell)} \leftarrow$  subsample from  $A^{(\ell-1)}$ 
49      $A_{j,2\delta}^{(\ell)} \leftarrow$  subsample from  $A^{(\ell-1)}$ 
50     for integer i from  $3\delta$  to  $A^{(\ell)}.i_{\max}$  by  $\delta$ 
51     {
52        $A_{j,i}^{(\ell)} \leftarrow$  update using the globally-4th-order scheme
53     }
54   }
55 }

```

Fig. 12 This figure gives an outline of the recursive-doubling algorithm for constructing extended initial data for the globally-4th-order initial data scheme. Coordinates for *all* grids are measured in units of the finest ($A^{(0)}$) auxiliary grid spacing, relative to the south corner of the problem domain. Thus, for example, the grid $A^{(3)}$ has spacing $2^3 = 8$ and uses grid-point indices $\{0, 8, 16, 24, 32, 40, \dots\}$.

The Newton’s-method solution is moderately expensive for a computation which (logically) is needed at each grid point: it typically requires 3–10 iterations, with each iteration needing an $\exp()$ computation and several other floating-point arithmetic operations. Fortunately, within any single grid r depends only on $j-i$, so in a unigrid code it’s easy to precompute r for all possible values of $j-i$ (of which there are only $\mathcal{O}(N)$ for an $N \times N$ grid) when the grid is first set up. For the slice-recursion algorithm a somewhat more dynamic “radius cache” of r coordinates is needed, with updates each time regridding grows, shrinks, or relocates a grid. However, the set of $j-i$ involved is still always a contiguous interval, so the cache bookkeeping overhead (over and above the storage arrays for the r coordinates themselves) is only $\mathcal{O}(1)$ per grid.

B.2 Local Coordinates for each Refinement Level

Consider a single slice, and a pair of adjacent grid points in it at some refinement level ℓ , say $G_{j,i}^{(\ell)}$ and $G_{j,i+1}^{(\ell)}$, viewed as events in spacetime. Since the grid spacing of $G^{(\ell+k)}$ is 2^k times finer than that of $G^{(\ell)}$, these same two events are necessarily 2^k grid points apart in $G^{(\ell+k)}$. This means that it’s impossible to define integer grid-point coordinates which simultaneously (a) have adjacent grid points separated by 1 in the integer coordinates at each refinement level, and (b) assign a given event the same integer coordinates at each refinement level.

In my AMR code I keep property (a), but discard property (b): each mesh-refinement level has its own local integer coordinate system for indexing grid points, and the code maintains explicit fine-to-coarse and coarse-to-fine coordinate transformations between each pair $(\ell, \ell+1)$ of adjacent refinement levels. These transformations are used when interpolating data from coarse to fine grids (discussed in detail in section B.3), when injecting fine-grid results back to coarse grids (lines 36–41 in figure 3), in setting up the “tail” re-integration (lines 43–48 of figure 3), and in checking the proper-nesting condition in regridding (lines 31–48 of figure 4). This scheme has worked very well, and I recommend its use to others implementing Berger-Oliger mesh-refinement codes.

However, for the extended-initial-data algorithm of figure 12, it’s convenient to use integer coordinates which keep property (b), but discard property (a). The CARPET code (Schnetter *et al.* (2004); Schnetter (2001)) also uses integer coordinates of this latter type.

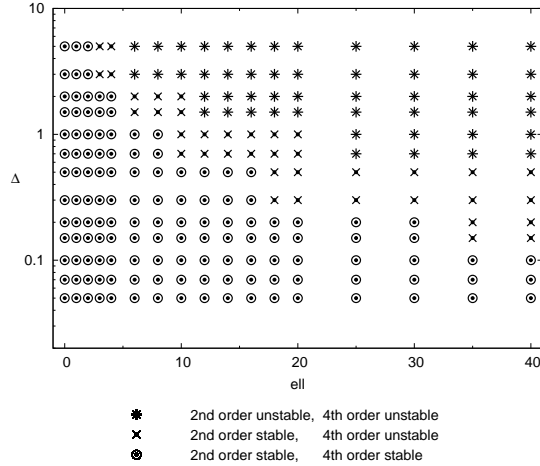


Fig. 13 This figure shows the stability behavior of unigrid evolutions with varying ℓ and Δ , using Gaussian initial data, no source term, and a problem domain size $D = 100M$. Notice that for each ℓ , the evolutions are always stable for Δ less than some threshold value.

B.3 Interpolation Operators

As discussed in sections 5.1 and 5.3, the slice-recursion algorithm needs to interpolate data from coarse to fine grids in several situations:

- When creating a new grid $G^{(\ell)}$, the first few slices (1 [3] slices for globally 2nd [4th] order finite differencing) of the newly-created grid are initialized by interpolating from the next coarser grid $G^{(\ell-1)}$ (line 20 of figure 4; figure 5c).
- When time-integrating any grid $G^{(\ell)}$ finer than the base grid, the extended initial data on each new $G^{(\ell)}$ slice (i.e., the first 1 [3] points on the slice for globally 2nd [4th] order finite differencing), must be interpolated from the next coarser grid $G^{(\ell-1)}$ (line 9 of figure 3; figure 5c,d). before the main integration of the slice can be started.
- When moving an existing grid $G^{(\ell)}$ to a new position in the current $v = \text{constant}$ slice, newly-created points are initialized by interpolating from the next coarser grid $G^{(\ell-1)}$ (lines 25–26 of figure 4).

As shown in figure 14, the precise choice of interpolation operator (which is made independently at each $G^{(\ell)}$ grid point) depends on the relative position of the $G^{(\ell)}$ interpolation point with respect to the next coarser grid $G^{(\ell-1)}$. All the interpolation operators considered here are Lagrange polynomial interpolants, which assume smoothness, so if the interpolation position is within a few grid points of the particle worldline (where ϕ is only C^1), then a different interpolation operator needs to be chosen so as to avoid crossing the particle worldline:

- If the interpolation point coincides with a coarse-grid ($G^{(\ell-1)}$) point, then the “interpolation” is just a copy of the data.
- Otherwise, if the interpolation point’s time (v) coordinate coincides with that of a coarse-grid ($G^{(\ell-1)}$) $v = \text{constant}$ slice, then the interpolation is a 1-dimensional Lagrange polynomial interpolation in space (u) within this slice, using 4 [6] points for globally 2nd [4th] order finite differencing. The interpolation is constrained not to cross the particle worldline and not to use data from outside the spatial (u) extent of the coarse slice. The interpolation is centered if this is possible within these constraints, otherwise it’s as minimally off-centered as is necessary to satisfy them.
- Otherwise, if the interpolation point’s spatial (u) coordinate coincides with that of a coarse-grid ($G^{(\ell-1)}$) $u = \text{constant}$ line of grid points, then depending on the relative position of the interpolation point and the particle worldline, there are two cases:
 1. If the interpolation point is not close to the particle worldline, then the interpolation is a 1-dimensional Lagrange polynomial interpolation in time (v) within the $u = \text{constant}$ line of coarse-grid ($G^{(\ell-1)}$) points, again using 4 [6] points for globally 2nd [4th] order finite differencing. The set of input points for this interpolation is always the most recent 4(6) slices of the coarse grid ($G^{(\ell-1)}$).
 2. Alternatively, if the interpolation point is too close to the particle worldline (i.e., if the 1-dimensional Lagrange polynomial interpolation molecule of case 1 would cross the particle worldline), then the interpolation is a 2-dimensional Lagrange polynomial interpolation in spacetime, chosen so as to not cross the particle worldline. This case is described further below.
- Otherwise (i.e., if the interpolation point lies in the center of a coarse-grid ($G^{(\ell-1)}$) cell), the interpolation is a 2-dimensional Lagrange polynomial interpolation in spacetime, again chosen so as to not cross the particle worldline. This case is described further below.

While it is straightforward to construct Lagrange polynomial interpolation operators in 1 dimension, doing so in 2 (or more) dimensions is more difficult. The basic concept is the same – an interpolating polynomial is matched to the known grid function values at some set of molecule points, then evaluated at the interpolation point – but there are several complications.

In 1 dimension the choice of interpolating polynomial is obvious, but in multiple dimensions different choices are possible. That is, let (v_*, u_*) be a fixed reference point somewhere near the interpolation point (v, u) , and define the relative coordinates $x \equiv v_* - v$ and $y \equiv u_* - u$. Then an n th degree interpolating polynomial in x and y might reasonably be defined as either

$$f(x, y) = \sum_{\substack{0 \leq p+q \leq n \\ p \geq 0, q \geq 0}} a_{pq} x^p y^q \quad (27)$$

or as

$$f(x, y) = \sum_{\substack{0 \leq p \leq n \\ 0 \leq q \leq n}} a_{pq} x^p y^q. \quad (28)$$

In my code I (somewhat arbitrarily) always use interpolating polynomials of the form (27). I use $n = 3$ [5] for 4th [6th] order LTE (corresponding to 2nd [4th] order GTE).

Given the choice of an interpolating polynomial, there are still many different molecules possible, even given the requirement that the values of the interpolating polynomial at the molecule points uniquely determine the polynomial coefficients. I have used the Maple symbolic algebra system (Char *et al.* (1983, version 11, <http://www.maplesoft.com/>)) to experiment with different interpolation molecules and to compute their coefficients. Figure 15 summarizes the set of spacetime-interpolation molecules used in my code. The actual coefficients may be obtained from the Maple output files in the `sfevol/coeff/` directory of the source code included in the electronic supplementary materials accompanying this article (online resource 2).

B.4 Data Structures

As noted earlier in this paper, the largest practical obstacle to the use of Berger-Oliger mesh refinement algorithms is the complexity of programming, debugging, and testing them. To help reduce this complexity for other researchers, here I briefly outline the main data structures and debugging/testing strategies I have found useful in implementing the slice-recursion algorithm.

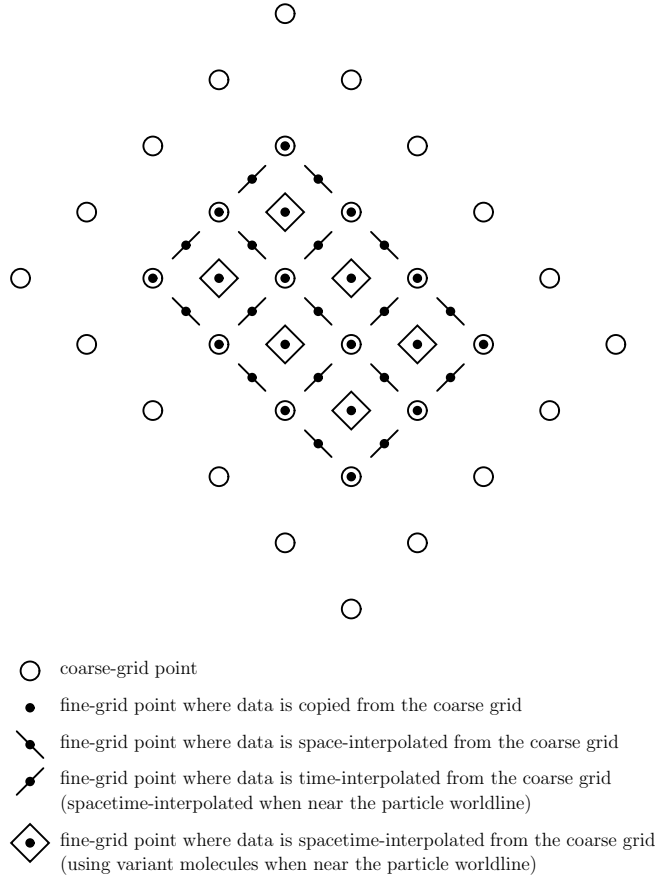


Fig. 14 This figure shows the type of interpolation operator used for each possible relative position of a fine-grid point with respect to the next coarser grid. The space-interpolation and time-interpolation operators are described in the text. The spacetime-interpolation molecules are shown in figure 15.

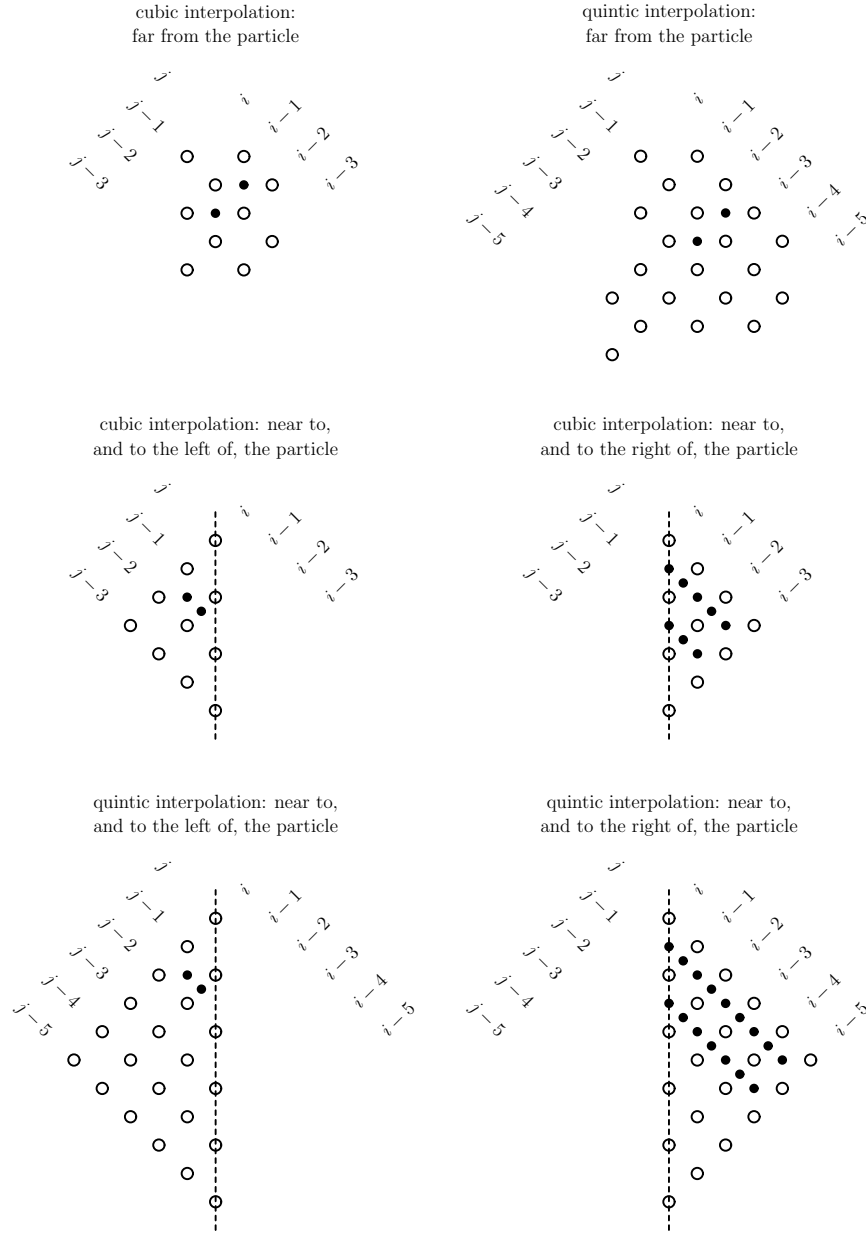


Fig. 15 This figure shows the spacetime-interpolation molecules. In each subfigure, the open circles show the input points of the interpolation molecule (some of which may have zero weight in any given molecule), the solid circles show the various interpolation points, and in the lower 4 subfigures, the dashed line shows the particle worldline.

A SLICE object represents a single $G_j^{(\ell)}$ slice at a single refinement level, i.e., it stores all the grid functions needed to represent the solution of the PDEs on that slice. In my code, SLICE is a C++ template with the template parameter selecting the PDE system (e.g., real or complex scalar field) to be supported.

A CHUNK object stores enough adjacent slices at a single refinement level to be able to take time steps, i.e., it stores 4 [7] adjacent SLICE objects for the 2nd [4th] order GTE finite differencing schemes described in this paper. CHUNK also maintains the radius cache discussed in appendix B.1. In my code, CHUNK is a C++ template with 2 template parameters, one selecting the PDE system and the other selecting the finite differencing scheme (2nd versus 4th order GTE) and thus implicitly the number of adjacent slices to be stored. To avoid unnecessary data copying, at each time step CHUNK circularly rotates pointers to a fixed set of SLICE objects. When debugging the code, CHUNK (and SLICE) can be thoroughly tested using unigrid evolutions.

A MESH object represents an entire grid hierarchy as described in section 5.1. That is, a MESH object stores a stack of CHUNK objects, one for each refinement level, together with the necessary bookkeeping information to compute the fine-to-coarse and coarse-to-fine coordinate transformations described in appendix B.2. When debugging the code, MESH can be tested by manually creating a grid hierarchy and testing that the expected results are obtained for various operations on it such as adding a new refinement level, dropping a refinement level, moving the chunk at some refinement level to a new location, interpolating or copying data from one refinement level to another, or transforming the per-refinement-level coordinates from one refinement level to another.

Finally, the actual slice-recursion Berger-Oliger and regridding algorithms are implemented in terms of the various MESH operations. I found it difficult to thoroughly test the Berger-Oliger and regridding logic, but this comprises a relatively small body of code – most of the overall complexity of the software lies in MESH and lower-level code, which is relatively straightforward to test.